International Journal of Plasticity 172 (2024) 103831

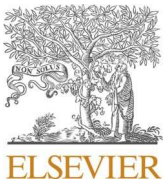

Contents lists available at ScienceDirect

International Journal of Plasticity

journal homepage: www.elsevier.com/locate/ijplas

Origin of thermal deformation induced crystallization and microstructure formation in additive manufactured FCC, BCC, HCP metals and its alloys

Jing Peng [a], Jia Li [a,*], Bin Liu [b], Qihong Fang [a,*], Peter K Liaw [c]

[a] State Key Laboratory of Advanced Design and Manufacturing for Vehicle Body, College of Mechanical and Vehicle Engineering, Hunan University, Changsha 410082, China
[b] State Key Laboratory of Powder Metallurgy, Central South University, Changsha 410083, China
[c] Department of Materials Science and Engineering, The University of Tennessee, Knoxville, TN 37996, USA

ARTICLE INFO

Keywords:
Additive manufacturing
Crystal structure
Alloying
Microstructure
Thermal deformation

ABSTRACT

The additive manufacturing (AM) technology has received the widespread attention in the industrial application because of its unique ability to achieve the complex shape and ideal performance. Unfortunately, the impact of the material natural characteristics, such as the crystal structure and alloying, on the microstructure formation at the nanoscale has never been revealed in AM metals. Here, we use large-scale molecular-dynamics simulations to study the rapid thermal deformation processes of additively-manufactured face-centered-cubic (FCC), body-centered-cubic (BCC), hexagonal close-packed (HCP) metals and their alloys (FCC Cu, $CuAl_{0.1}$, BCC Fe, $FeAl_{0.1}$, and HCP Mg, $MgAl_{0.1}$) in the molten pool, in an attempt to elucidate the intrinsic physical mechanisms controlling the crystal nucleation and growth under the complex thermal stress. The results show that the arcuate solid-liquid interface migrates towards the liquid phase until the complete crystallization, in good agreement with the experimental observation. The solidification rate follows a unified slow-to-fast law in the three types of metals, due to the competition between the compressive thermal stress and fast atomic motion. It is noteworthy that the critical radius of the crystal nucleus in the FCC and BCC metals is smaller than that in the HCP metal. The FCC metal exhibits the weak nucleation ability and growth rate, and yet the HCP metal shows the fast growth rate and stable columnar crystal nucleation. Especially, due to the dual regulation of the steep thermal gradient and solute redistribution on the growth driving force, the alloying increases the constitutive supercooling of the solidification front and inhibits the growth of columnar crystals. This trend is particularly prominent in FCC alloys, which is manifested by the obvious amorphous phase and discrete nucleation point in the upper part of the melt pool. The nucleation barrier free energy descends in order of FCC, BCC, and HCP pure metals, but the alloying would increase this energy in the corresponding alloys. The current work gives an insight into the atomic mechanism of the nucleation and growth in AM FCC, BCC, and HCP metals.

* Corresponding authors.
E-mail addresses: lijia123@hnu.edu.cn (J. Li), fangqh1327@hnu.edu.cn (Q. Fang).

https://doi.org/10.1016/j.ijplas.2023.103831
Received 6 September 2023; Received in revised form 28 November 2023;
Available online 1 December 2023

1. Introduction

The additive manufacturing (AM) technology can realize the integrated forming of components with complex shapes. The AM technology has become the frontier direction of the aviation manufacturing in recent years (Blakey-Milner et al., 2021; Hashemi et al., 2022; Ren et al., 2022; Zhakeyev et al., 2017; Zhao et al., 2021), which is difficult to achieve by the traditional manufacturing methods. Numerous studies suggest that the target materials with superior performance are obtained through the certain designs in AM. For instance, the heterogeneous alloy is formed by modulating the concentration of the two alloy melt using a laser powder bed fusion technology (Zhang et al., 2021b). The AM-fabricated heterogeneous Ti alloy exhibits high tensile strength and uniform elongation, overcoming the problem of poor work hardening ability in a single alloy. In the AM-fabricated CoCrFeNiMn high entropy alloy, the dendritic grains at the edge of the molten pool transits to the equiaxed grains at the center under the action of a directional solidification (Chew et al., 2019). The grain boundary strengthening is enhanced due to the grain refinement (Chew et al., 2019). Meanwhile, the unique dislocation-cell structure produced by AM is also an important factor in improving the strength of materials (Joshi et al., 2023; Li et al., 2020a, 2021b, 2020d).

However, there are still some difficulties to be overcome for achieving the widespread application of AM technology. Under the influence of the complex thermal stress and thermal deformation generated by the steep temperature gradient up to 10^6 K/m (DebRoy et al., 2019, 2018; Oliveira et al., 2020), the residual stress, the microcrack, the columnar crystal, and the elemental segregation are inevitable, which may reduce the plastic properties (Fu et al., 2021; Huang et al., 2022; Sui et al., 2022; Zhang et al., 2019a). Currently, some strategies have been adopted for defect suppression and microstructure regulation in AM metal. For example, the grain refinement enhances the strength and reduces the hot cracking in the Zr-modified AlCuMg alloy (Zhang et al., 2017). The addition of Ti element suppresses the segregation in the FeCoCrNi multicomponent alloys, and then improves the tensile strength and corrosion resistance (Fujieda et al., 2019). Thus, the elements distribution at the solidification front results in a modification of solidification temperature that produces high constitutional undercooling to promote the formation of equiaxed crystals. In addition, the local microsegregation with a slightly lower melting point increases the nucleation sites, which reduces the effect of the high temperature gradient and disrupts the growth of columnar crystals (Ghoncheh et al., 2020; Oliveira et al., 2020). Hence, the composition modification and design have made some progress in the development of new alloys. Meanwhile, the nucleating agent nanoparticles promote the transformation from the large columnar crystals to the equiaxed crystals, thereby alleviating the anisotropic mechanical properties and the hot microcrack formation (Gong et al., 2021; Li et al., 2020c). Besides, optimizing the AM parameter is regarded as the other important strategy to control the microstructure for improving the performance (Ghorbanpour et al., 2022; Liu et al., 2020; Wang et al., 2019). A new AM technology combined the laser shock peening with the laser powder bed fusion has been proposed to achieve the microstructure customization (Lu et al., 2023). These methods have preliminarily solved the challenges of molding and microstructure regulation in AM. However, the component regulation and the process improvement rely on a large amount of experience and verification. The type of the nucleation agent is also limited. Whether it is possible to find the certain rules to guide the forming and properties of AM, is a research goal in this field. Thus, it is crucial to investigate the thermal deformation including the thermal expansion and contraction of the melt pool induced by the melting and solidification processes. This work not only reveals the intrinsic physical mechanism of thermal deformation on solidification and microstructure formation under the non-equilibrium conditions, but also accelerates the development of AM technology. The evolution of the microstructure has been investigated under a non-equilibrium solidification condition in the AM process (Bandyopadhyay et al., 2022; Liu et al., 2022b; Tang et al., 2021). The grain morphology including the columnar crystals, equiaxed crystals, dendrites, and cellular crystals in AM-fabricated alloy relies on the relationship between thermal gradients and the growth rate of solid-liquid interface (Liu et al., 2022b; Oliveira et al., 2020). Nevertheless, there is still a lack of the underlying physical mechanism of the dynamic solidification based on the intrinsic characteristics of metals, due to the difficulty in tracking the dynamic impact of the thermal stress evolution on the structural formation.

As we all know that many properties of the metals are closely related to their crystal structures. According to previous studies, there are obvious effects of the crystal structures on the mechanical behavior (Chung et al., 2023; Picard and Sansoz, 2022; Varillas et al., 2021). The nanocontact plasticity is systematically investigated by MD simulations of the nanoindentation behavior in different crystallographic structures, which reveals the nanoimprint-formation mechanism in FCC, BCC, and HCP metal (Varillas et al., 2021). The difference of the Ni elemental segregation behavior at the grain boundary in some alloys with different crystal are studied. Unlike the heterogeneous segregation in the FCC alloy, the homogeneous segregations in BCC and HCP alloys are observed (Picard and Sansoz, 2022). Meanwhile, it was found that after thermal deformation involving atomic diffusion and contraction during non-equilibrium solidification, the crystal structure has a significant impact on the forming and mechanical properties of printed metals (Khodabakhshi et al., 2020). Comparing the microstructure and mechanical property of the austenitic steel and martensitic steel prepared by AM, the equiaxed grains of AM-fabricated martensitic steels are sharply refined, and the strength is significantly improved, compared with the traditional commercial martensitic steels. The AM-fabricated austenitic steel is deposited into a coarse columnar structure, and its strength is greatly reduced (Khodabakhshi et al., 2020). As we all know, the high intragranular residual stress is a thorny issue in AM-fabricated metals, which often affects the mechanical properties of components (Balbaa et al., 2020; Papanikolaou et al., 2022). The high residual stress at the fusion zones between the grains is the main reason for the formation of the long and straight thermal cracks at the grain boundaries (Guo et al., 2023). Interestingly, when the crystal structure of powder change from BCC to FCC, the residual stress is reduced and the deformation mechanism is adjusted, thereby suppressing the thermal cracking of printed alloy and improving its strength (Niu et al., 2023). Thus, the crystal structure is a key factor affecting properties. Nonetheless, the intrinsic differences of the solidification molding dominated by the crystal structures have not yet been revealed.

In addition, the solubility of solutes in the solid and liquid phases is different during the non-equilibrium solidification process of alloys, which leads to the redistribution of elements induced by thermal deformation process of the melting and solidification. For

example, the chromium-rich carbides precipitate in a GCr15 steel, owing to the redistribution of solutes at the solidification interface and the occurrence of segregation between liquid-phase dendrites (Wang et al., 2023b). The influence of gas pore and element redistribution on the vertical solidification process of the Al-Cu alloy has been studied, which found that an appropriate amount of hydrogen can reduce the reverse segregation of the Al-Cu alloy (Gao et al., 2019). The eutectic structure generated by the solute redistribution during the solidification process of the Al-Si alloy can achieve better mechanical properties after the heat treatment (Li et al., 2015). However, the influence of element concentration fluctuations induced by thermal deformation in the molten pool on the formation of printed microstructure is still unclear.

In order to reveal the intrinsic physical mechanism of AM, the dynamic-formation process of the microstructure and the details of the crystals nucleation still need to be further explained. However, the experimental methods are challenging. With the development of the technology, in-situ electron microscopy, neutron scattering, and in-situ high-energy X-ray diffraction are used to dynamically observe the rapid solidification process and to understand the interaction among the laser and material (Dai et al., 2020; Yao et al., 2019). For example, the solid-liquid interface instability and the transformation of the solidification growth mode of the Al-Cu alloy are observed through in-situ electron microscopy (McKeown et al., 2014). The in-situ high-energy X-ray diffraction and the multi-physical field simulation are combined to reveal the surface morphology and pore-forming process (Leung et al., 2018; Martin et al., 2019). However, it is hard to (i) observe the real-time transition from liquid phase to crystalline phase, as well as the dynamic growth process of grain at the atomic scale; (ii) obtain the intrinsic mechanism of nucleation and growth by the direct experimental method.

Thus, based on the solidification-dynamics theory, a series of simulation methods, such as the finite element (Hu et al., 2022; Keller et al., 2017; Liu et al., 2022a), phase field (Ji et al., 2023; Liu et al., 2022a), and MD (Mahata et al., 2022a; Peng et al., 2023a; Kurian et al., 2020), are used to simulate the solidification dynamic forming process. Among them, MD simulation can be used to analyze the directly thermal deformation details at atomic scale. Importantly, this method can realize the advantage of the direct control of the temperature in the melt pool both spatially and temporally based on the experimental observation, and then provides a fundamental atomic scale understanding AM process, finally contributes to optimize AM parameters. The homogeneous nucleation process of the pure metal with different lattices has been studied by MD simulations, which found that the orientation difference between two nuclei separated by the grain or twin boundary leads to heterogeneity in the homogeneous nucleation process (Mahata et al., 2022a). Based on the atomic-scale elemental segregation characterized by experiments, the evolution law of elements is revealed by the atomic-scale simulation method during the dynamic growth process of columnar crystals (Peng et al., 2023a). Meanwhile, the change law of microstructure defects and surface morphology affected by the scanning rate and laser energy is obtained (Peng et al., 2023b). By simulating the process of melting and solidification of the randomly distributed Al nano-powder bed, the epitaxial grain growth induced by adjacent molten pool and previous layers is observed (Kurian et al., 2020).

In the present work, the intrinsic physical mechanisms of the crystallization and microstructure formation induced thermal deformation in AM-fabricated FCC, BCC, HCP pure metals and their alloys are investigated. The melting and solidification processes are directly observed from the atomic scale using the MD simulations. The columnar crystal growth morphology, microstructural defect, and residual stress of the AM samples are compared by considering the thermodynamic driving force in the pure metal, and the thermodynamic/chemical driving force in the alloys. The differences of the nucleation barrier energies in different lattice structures are revealed during the dynamic crystallization process.

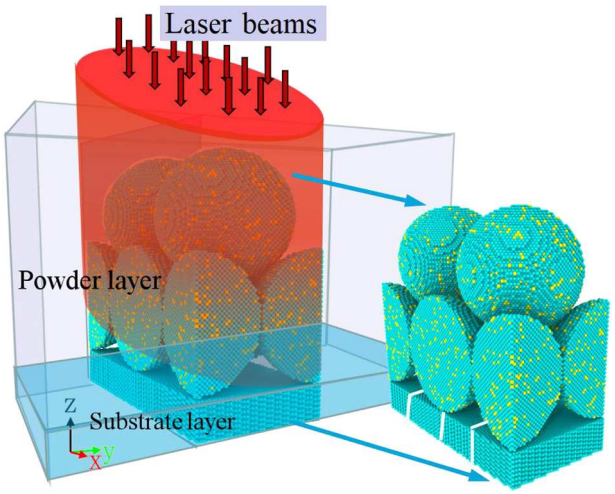

Fig. 1. The diagrammatic sketch of the powder bed.

2. Method

2.1. Atomic modeling and potential

The present work is devoted to investigating the influence of crystal structure and alloying on the microstructure forming after thermal deformation of melting and solidification during the AM process by MD simulations. Firstly, three local powder beds are set, respectively, with FCC Cu, BCC Fe, and HCP Mg as raw materials. The powder bed includes the substrate and two layers of spherical powder with a radius of 5 nm. The second layer of powder is set in the gap of the first layer to meet the actual requirements for the compactness of the powder bed. The substrate materials are set to the same Cu, Fe, and Mg as the powder material, respectively. To study the alloying effect, the same Al concentration with 10 % is introduced into three pure metals, the Al atoms are randomly distributed to correspond to the alloy powder, and thus a $CuAl_{0.1}$ ($FeAl_{0.1}$ and $MgAl_{0.1}$) alloy powder bed is established on the basis of the Cu (Fe and Mg) substrate. The built alloys generate different initial stress states due to the lattice and modulus mismatch. However, during the AM process, the structure undergoes a complete melting and solidification process, thereby eliminating the effect of initial stress generated by the introduction of Al element.

The substrate of each sample with size of 20 nm × 10 nm × 2.8 nm is composed of four grains with the same geometry but different orientations. The substrate is set as the boundary layer, thermostat layer, and Newton layer from bottom to top, and the thickness is 5 Å, 5 Å, 18 Å, respectively. The boundary layer is set to fix the substrate and eliminate motion; the thermostat layer is kept 293 K, using the velocity-rescaling method to simulate the heat dissipation of the substrate. The Newton layer is set with initial temperature of 293 K, and the atomic motion in this layer follows the classical Newton's second law. The Newton layer is used as a transition between powder and the thermostat layer to avoid excessively high temperature gradients at the bottom of molten pool. Based on the characteristics of complete melting of the powder bed in the AM process, the influence of powder orientations on the forming will not be considered, thus the powder orientations are uniformly set. The diagrammatic sketch of powder bed of is shown in Fig. 1. The atomic model indicated by the arrow is the simulation scope in the present work. For the whole model, the shrink-wrapped boundary conditions are applied in the z direction. The periodic boundary conditions are set along the x direction and y direction to eliminate finite system effects and model an infinite array of particles. These models are set to an initial temperature of 293 K, and they are relaxed under the microcanonical ensemble (NVE) combined with temperature control to obtain a stable initial configuration. The modified embedded-atom method (MEAM) atomic potential has been employed to describe the interaction between each atomic pair, Cu-Cu, Cu-Al (Mahata et al., 2022b), Fe-Fe, Fe-Al (Mahata et al., 2022b), Mg-Mg, and Mg-Al (Dickel et al., 2018). These atomic potentials can accurately evaluate the melting point, elastic constants of materials as shown in supplementary file (Table S1). The entire simulation process is based on a large-scale atomic/molecular massively parallel simulator (LAMMPS) (Plimpton, 1995).

2.2. Melting point

To compute the melting point, the cube models with size of $10a \times 10a \times 10a$ are established for the pure metals and the binary alloys, where a is lattice constant. The temperature of the model is increased from 300 K to 2000 K under the constant temperature and constant pressure ensembles using the MEAM potential in the present work. The melting point is the temperature corresponding to a sudden change in potential energy. In addition, using the rule of mixture (Senkov et al., 2010), the theoretical melting point of alloys can be calculated as $T = \sum_{i=1}^{n} c_i T_i$, where c_i is the atomic percentage, and T_i is the melting point of each element (Kaptay, 2012; Mahata et al., 2022b). The related temperature is listed in Table 1. It suggests that the current simulation results are consistent with previous experiments and theoretical calculations.

2.3. Additive manufacturing simulation

In order to simulate the action of laser on powder and the rise of molten pool temperature, the "fix ehex" command in LAMMPS is used. This is an improvement of the "fix heat" command, which can effectively reduce thermal drift. The laser heating process is simulated by adding non-translational kinetic energy to the atoms in the powder area at a fixed rate (Jiang et al., 2021, 2020; Zhang et al., 2019b). The parameter of energy input in the simulation is set to 1000 ev/ps, corresponding to the laser power of nearly 160 μW, and the fluence of 7.8×10^{11} W/m^2 (Fig. 1). The laser region is set with the size of 20 nm × 10 nm × 19 nm. The depth is slightly higher than the top of the powder bed, and the model is fully covered by the laser in both the x and y directions. With the aim of ensuring complete melting of the powder and avoid splashing of the upper layer atoms due to high temperature, the energy is uniformly added to the molten pool by the laser region and independent of spatial position in the present work. When the average temperature of the molten pool rises to near the melt temperature, Tm, there are still a few crystalline atoms. Thus, the energy is continuously input until the average temperature of the molten pool reaches 1.4 to 1.5 Tm to ensure that the powders are completely melted, and the different

Table 1
The temperature parameters of the material (Kaptay, 2012; Mahata et al., 2022b; Valencia and Quested, 2001).

Material type	Cu	Fe	Mg	$CuAl_{0.1}$	$FeAl_{0.1}$	$MgAl_{0.1}$
Theoretical melting point (K)	1357	1811	923	1315	1723	924
Calculated melting point (K)	1390	1980	1150	1378	1850	1050
Peak value of molten pool temperature (K)	2151	2508	1519	2100	2602	1520

materials reach the same melting state. The corresponding melting point and the average temperature of the molten pool are shown in Table 1. Hence, the duration of energy input is set as 140 ps for FCC Cu, $CuAl_{0.1}$, 200 ps for BCC Fe, $FeAl_{0.1}$, and 60 ps for HCP Mg, $MgAl_{0.1}$ under the same laser power. Subsequently, the energy input is stopped, and the molten pool is cooled to room temperature under the effect of substrate thermal diffusion of the substrate constant temperature layer, which corresponds to the natural cooling process induced by the substrate. The time step of the solidification process of all simulation cases is set to 0.001 ps. In order to avoid the influence of randomness on the results, we carried out five repeated simulations by changed the random parameters controlling the atomic position and also adjusted the grain orientation in the substrate. Part of the simulation results are presented in supplementary file.

2.4. Microstructure identification

To directly describe the influence of the crystal structure and alloying effect on the grain growth morphology, microstructure, and residual stress under the complex thermal stress, we conducted a series of post-processing, using the open visualization tool (OVITO) (Stukowski, 2009). A common neighbor analysis (CNA) method is used to better distinguish the crystal structure (Tsuzuki et al., 2007), the different crystal structures are marked with different colors, e.g., FCC structure is marked with green, a HCP structure is indicated with red, a BCC structure is represented with blue, and the liquid and amorphous structure is denoted with gray. The dislocation is identified by the dislocation extraction algorithm (DXA) method (Stukowski and Albe, 2010).

3. Results

3.1. Effect of crystal structure on microstructure formation

In order to investigate the influence of the crystal structure on the AM formation, the dynamic growth behavior of a columnar crystal in the FCC Cu, BCC Fe, and HCP Mg during the melt pool deformation are compared, and the marked difference is revealed in Fig. 2. Herein, the solidification states are dived into the initial solidification, grain growth to half the height of the melt pool, and the end of solidification. The original solid in the molten pool absorbs the heat, expands with the injection of the energy, and melts into a liquid state. When the molten pool is initially cooled owing to the heat dissipation of the substrate, the temperature gradient between the substrate and molten pool is steep (Song et al., 2021), and the columnar crystal near the substrate begins to grow in the FCC Cu.

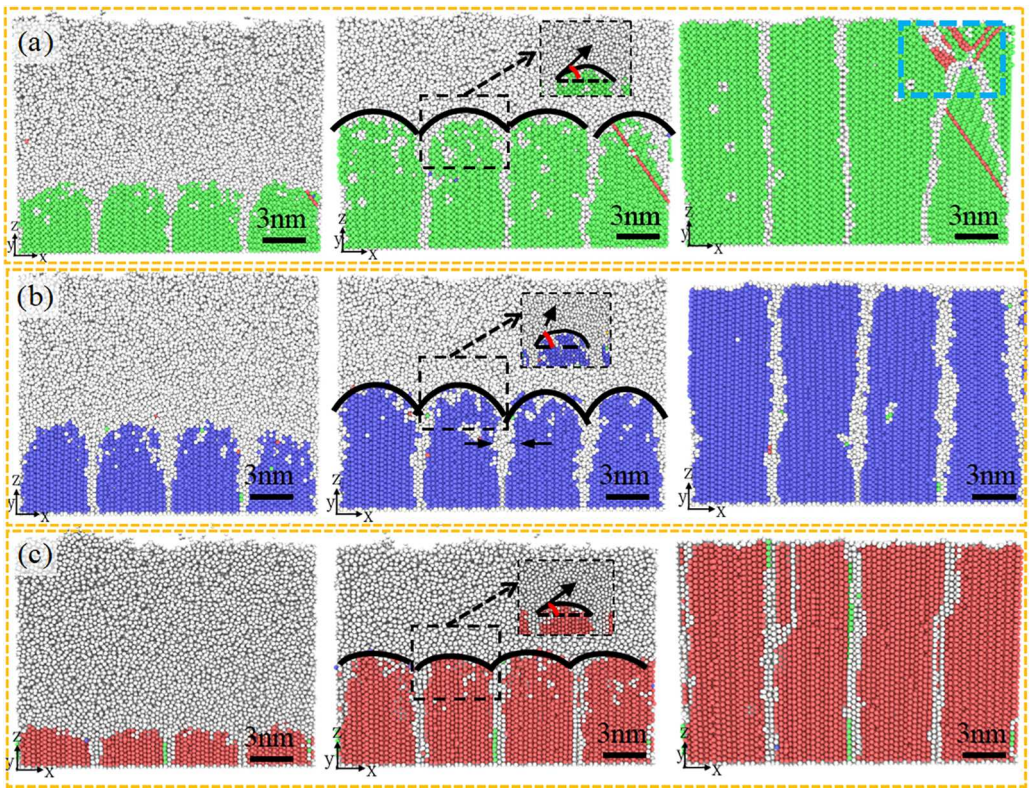

Fig. 2. The states of columnar crystal growth at the initial, middle, and final stages of solidification for Cu (a); Fe (b), and Mg (c). The atomic colors are defined by CNA, where green atom denotes FCC structure, blue atom represents BCC structure, red atom is HCP structure, and gray atom is liquid, and gran boundary. The black arcs represent the outline of the solidification front.

Similarly, the early growth occurs in the BCC Fe. However, this phenomenon has not been observed in the HCP Mg.

The outline of the solidification front and the morphology of the solid-liquid interface are represented by the black arcs in Fig. 2 (a–c), which can be obtained by the DXA method, and the relevant details are stated in supplementary file. The solid-liquid interface stands for the boundary between crystalline and amorphous structure identified by CNA method. The solid-liquid interface protrudes upward in the middle of the grain, and bends downward near the grain boundary. It indicates that a large surface tension is generated under the effect of a large thermal gradient, which causes the Marangoni vortex in the molten pool and induces particle movement (Wang et al., 2023a). However, by comparing the morphology of the solid-liquid interface in the molten pool, the arc curvature exhibits the obvious discrepancy among three crystal structures, which are determined by the direction of the thermal gradient and the capillarity (Xing et al., 2022). Compared with different crystal structures, the curvature of the interface contour in Cu and Mg is small, meaning that the longitudinal thermal gradient dominates the growth process. The large curvature in Fe is attributed to the strong radial thermal gradient. Normally, the atoms bear the compressive thermal stresses in the heat zone (Chen and Yan, 2020). As the heat dissipates, the atom spacing decreases under the compressive thermal stress until the thermal motion cannot overcome the bonding force between atoms. The solid-liquid interface reflects the direction of both the thermal gradient and compressive thermal stress. In other words, the longitudinal compressive thermal stress promotes the smooth advancement of the growth interface. In addition, the arc-shaped solidification front is considered as a spherical coronal nucleus, as shown in the black dashed box. The formed solidification area would serve as the crystal nucleus on the substrate. According to the classical nucleation theory, the critical radius of the crystal nucleus is expressed as (Jafary-Zadeh et al., 2018; Porter et al., 2021):

$$r^* = \frac{2\sigma_{\mathrm{LC}} \cdot T_{\mathrm{m}}}{L_{\mathrm{m}}\Delta T} \tag{1}$$

The nucleation barrier energy required to form a critical radius is (Kashchiev, 2000; Yousefian and Tiryakioğlu, 2018)):

$$\Delta G^* = \frac{16\pi\sigma_{\mathrm{LC}}^3 T_{\mathrm{m}}^2}{3L_{\mathrm{m}}^2(\Delta T)^2}\left(\frac{2-3\cos\theta+\cos^3\theta}{4}\right) \tag{2}$$

where σ_{LC} is the interfacial free energy between the crystal nucleus and liquid phase. For the metal, $L_{\mathrm{m}}/T_{\mathrm{m}} = \Delta S_{\mathrm{m}}$ is the melting entropy, approximately a constant. L_m is latent heat of melting. ΔT is the degree of supercooling, θ is the wetting angle between the

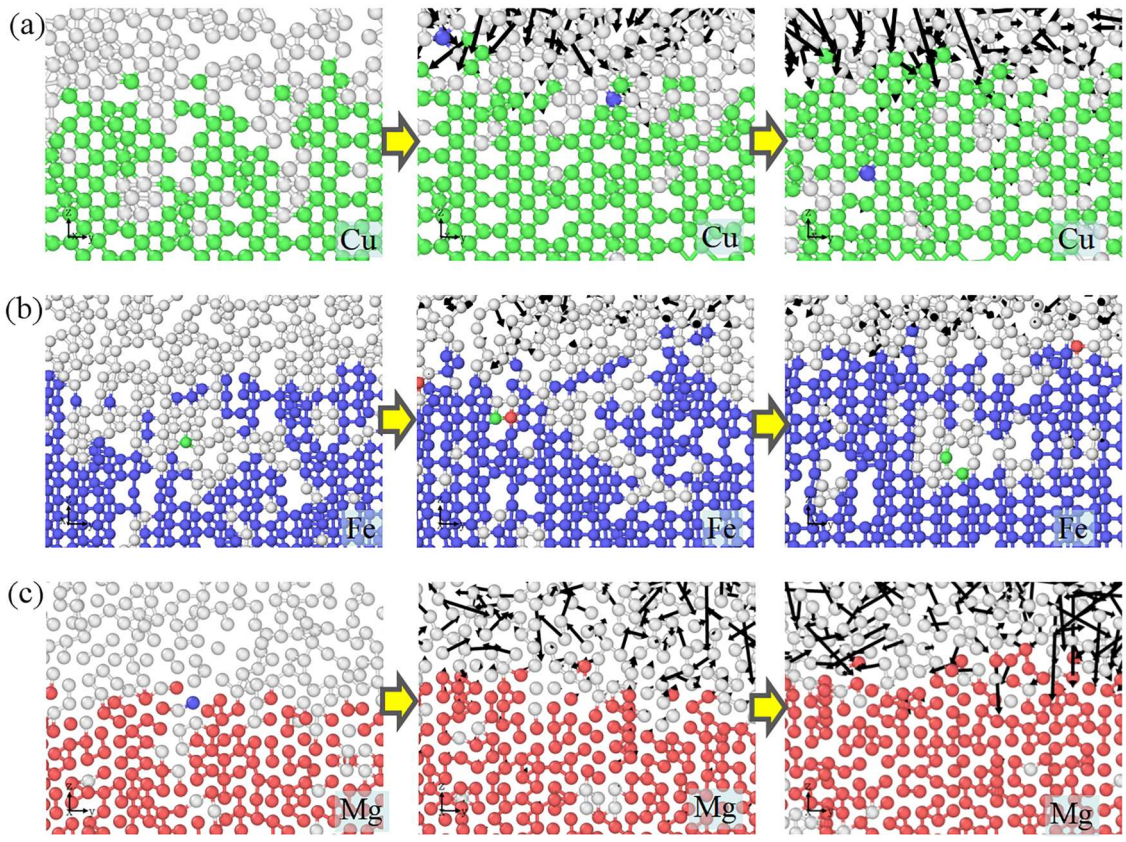

Fig. 3. Snapshot of local atomic motion during solidification process. (a) for Cu, (b) for Fe, and (c) for Mg. The black arrow indicates the direction of atomic motion.

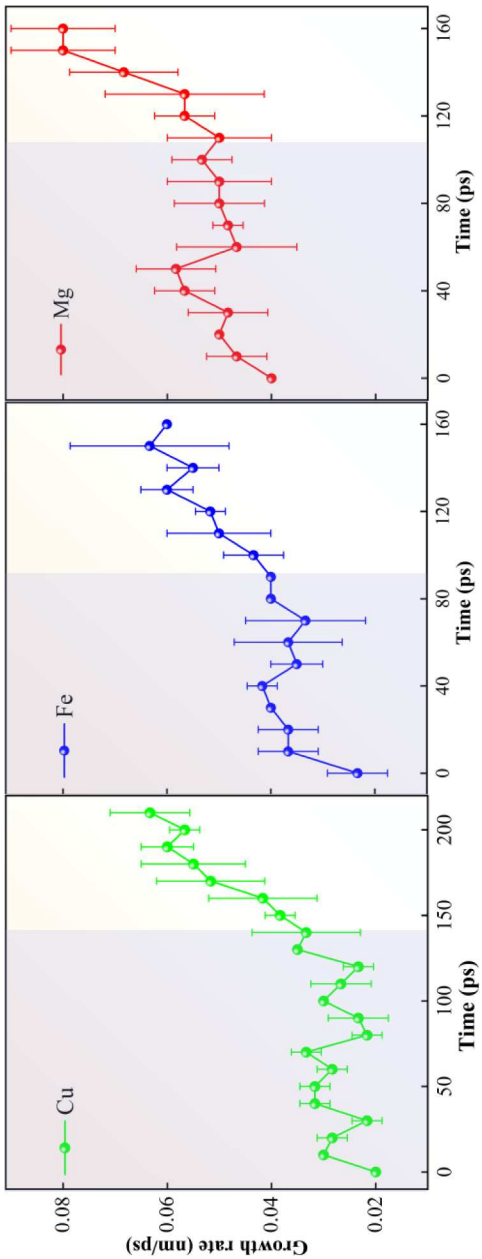

Fig. 4. The average growth rate of solid-liquid interface for Cu, Fe, and Mg.

crystal nucleus and substrate, as shown by the red solid line in Fig. 2. The smaller wetting angle would lead to the better wettability of the solid liquid two phases (Tan et al., 2022). However, the wetting angle is hardly measured through the experiments. It can be found that the wettability of the FCC Cu and HCP Mg is slightly better than that of the BCC Fe. The difference of the wetting angle is affected by the surface tension generated from the mutual arrangement of atoms at the solid-liquid contact surface. Meanwhile, the small wetting angles reflect the heterogeneity in the homogeneous nucleation of pure metals (Mahata et al., 2022a).

According to the previous studies (McLouth et al., 2020; Wei et al., 2016), the prior growth direction is parallel to ⟨100⟩ during the solidification process in the metals. This is related to the fact that the direction of ⟨100⟩ is the least tightly packed. When the influence of the lateral epitaxial growth is negligible, the growth direction of columnar crystal is parallel to the heat flow direction and perpendicular to the tangential direction of the molten pool boundary (Xu et al., 2021). In the present work, the ⟨100⟩ crystal orientation along z-direction is adopt, which is the prior growth of the FCC and BCC metals; the $\langle 11\bar{2}0\rangle$ crystal orientation along z-direction is adopt in HCP structure. It can be observed that the competitive epitaxial growth occurs in the middle and late stage of solidification in the FCC Cu as presented in the blue box of Fig. 2(a). The grain growth direction is perpendicular to the ⟨100⟩. There is almost no the competitive epitaxial growth in the BCC Fe (HCP Mg), and the columnar crystals grow parallel to the ⟨100⟩ ($\langle 11\bar{2}0\rangle$ for Mg) along the z-direction. The dynamic crystallization and motion process of local atoms are shown in Fig. 3. The atoms in the liquid phase represent significant large spacing and disorder. The atoms sink due to the effect of the temperature gradient and the compressive thermal stress, until a stable metallic bond is formed. It is worth noting that the final stable structure is not formed at one time, but undergoes the multiple thermal deformation. The phenomenon is hard to be observed by other experiments and simulation method up to date.

The average growth rates (R) of the solid-liquid interface are obtain by counting the average growth rate in our repeated simulation results, which are exhibited in Fig. 4. The growth rate depends on the thermal environment of molten pool. Due to the extremely high initial temperature of molten pool, it is difficult to achieve the required supercooling for solidification, even under the influence of high temperature gradients (G). The atomic thermal motion is difficult to be overcome by the compressive thermal stress, and the stable bonds cannot be formed between atoms. Thus, the solid-liquid interface growth rate is low at the first half stage. As the solid-liquid interface advances and the molten pool shrinks, the thermal deformation of atoms slows down due to the temperature and its gradient decrease in molten pool. The bonds between the atoms can be formed quickly, leading the solid-liquid interface growth rate rapidly increases. The growth rate obey the unified law of slow followed by fast in all three metals, which is in good agreement with the results in previous studies (Raghavan et al., 2016). In addition, the relationship of G and R is crucial for the grain morphology (Li et al., 2020a, 2022). The value of G/R decrease at the second half stage of solidification, the columnar grain growth is inhibited in the FCC metal (Fig. 2(a)). Meanwhile, a significant discrepancy can be captured. The growth rate of Cu remains below 0.0375 nm/ps before 150 ps, and the trend is relatively stable. After 150 ps, the growth rate exhibited a sharp increase. Similarly, the solidification rate of the BCC Fe also shows two different stages before and after 90 ps. A relatively stable stage is maintained before 90 ps, and the growth rate increases rapidly at the later stage. However, for the HCP Mg, the solidification rate at the initial stage is higher than that in Cu, and Fe. After 110 ps, the growth rate continues to rise, and the overall average rate in Mg is highest among the three metals. The difference of these growth rates is mainly caused by the inconsistent thermodynamic driving forces of different crystal structures

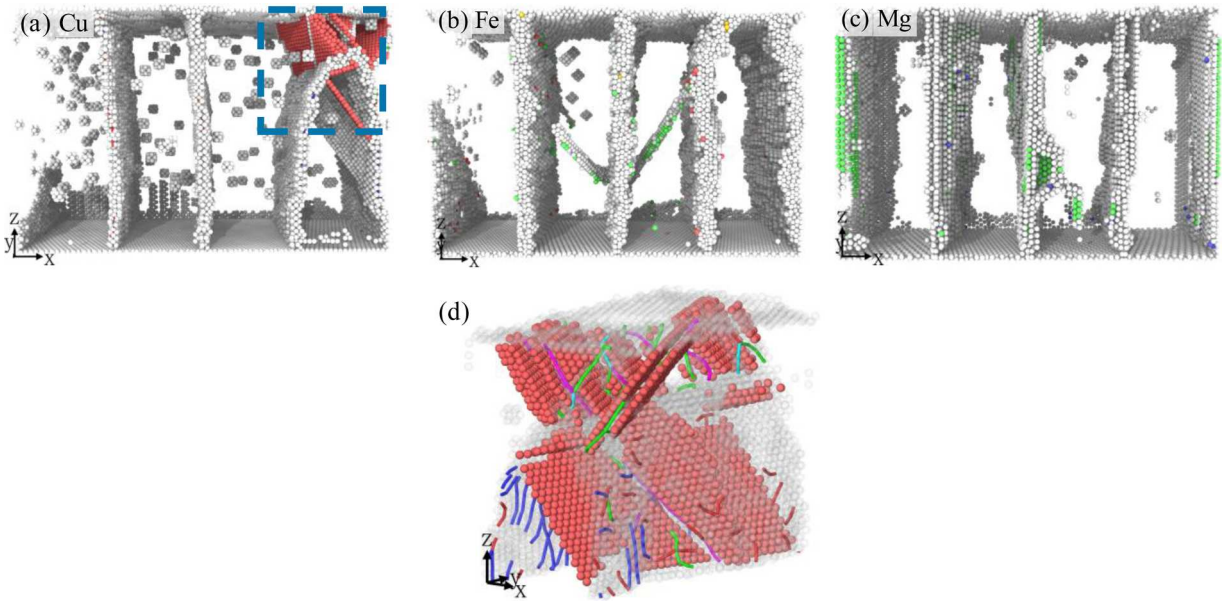

Fig. 5. The microstructure defect in AM-fabricated (a) Cu, (b) Fe, and (c) Mg. The typical defects are highlighted in (d). Here, the green line represents the 1/6<112> Shockley dislocation, the pink line is the 1/6<110> stair-rod dislocation, the blue line denotes the 1/6<110> perfect dislocation, the sky-blue line is the 1/3<111> frank dislocation, and the red line is other dislocation.

during solidification (An et al., 2022; Martin et al., 2020).

The defect structures are obtained by removing the perfect lattice, as shown in Fig. 5. The thermal stress history would be retained in the microstructure defect. As the solid phase forms, the planar defects, such as stacking fault and twin, take place under the effect of the significant thermal stress or the supercooling at the solid-liquid interface (Wang et al., 2018a). In our atomic simulations, the stacking faults and twins appear at the lateral epitaxial growth grains. The grain-orientation competition and the solid-liquid phase transitions leads to the high local stress concentration, and thus provide a driving force for the nucleation of stacking fault and twin (Lv et al., 2022). However, the obvious plane defects are not observed in BCC Fe and HCP Mg due to their high critical nucleated stresses in comparison with FCC Cu. In addition, the vacancy is one of the defects produced during the repeated thermal deformation process of lattice structure (Xu et al., 2020). A large number of the discrete vacancies are observed in the grains of Cu, but only sporadic vacancies occur in Fe and Mg. During the growth process, the amorphous structure between the columnar crystals is wider, leading to the formation of a thick grain boundary in the BCC Fe. However, the grain boundary of the HCP Mg is regular and straight. Some FCC phases are observed at the grain boundaries in Mg. Due to the orientation mismatch between grains, many dislocations nucleate at grain boundaries. According to the statistical results of DXA, the dislocation length in the grain boundary of the FCC Cu, and HCP Mg are 662.8 nm, and 391.8 nm, respectively. No dislocations are identified in the grain boundary of the BCC Fe, attributed to the more relaxed and disordered distribution of the atoms from grain boundary (Żydek et al., 2021).

During the AM process, the stress distribution is complex due to the repetition of thermal expansion and contraction. The residual stress can reflect thermal stress history. However, it is hard to display the stress state of solidification structure through only one stress component. Thus, the von Mises stress and the mean stress are used to estimate the AM sample after cooling to room temperature in different crystal structure, exhibited in Fig. 6. For the von Mises stress (Fig. 6a–c), there is a significant distinction between the intergranular residual stress and the intragranular residual stresses. The former is markedly higher than the latter. There is the high stress at grain boundary and the large stress gradient between grain boundary and grain interior, which are the root cause for the cracks in the printed metals (Guo et al., 2023; Sun et al., 2022). Furthermore, the width of the high stress zone is almost completely corresponding to the width of the grain boundary, which is the largest in the BCC Fe. Besides, the distribution of mean stress is exhibited in Fig. 6 (d–f). Obviously, the rule of distribution of the mean stress is consistent with that of the von Mises stress. There is the positive mean stress at grain boundary, and the value is high. The stress inside the grain is small, and local areas show negative stress values. Thus, the macroscopic stress balance is satisfied. For the overall structure, the residual stress in the HCP Mg and FCC Cu is lower than that in BCC Fe. The local stress in the cooling process induces the martensitic transformation (the HCP phase) and reduces the residual stress (Li et al., 2021a; Richter et al., 2022). Therefore, the multiple phase transformations is an effective mechanism to reduce residual stress (Guo et al., 2023; Richter et al., 2022). This is consistent with the previous work, which can control the residual stress by changing the crystal structure of the powder (Niu et al., 2023).

3.2. *Effect of alloying on microstructure formation*

The alloying effect in different crystal structures on the solidification is further studied. The dynamic growth process of the columnar crystal is different among the FCC $CuAl_{0.1}$, BCC $FeAl_{0.1}$, and HCP $MgAl_{0.1}$ alloy (Fig. 7). Similar to the pure metal, the early growth of the columnar crystal is observed in the $CuAl_{0.1}$, and $FeAl_{0.1}$ alloys at the initial solidification stage.

By observing the solid-liquid interface front at the middle stage of solidification, the arc curvature at the solidification front of the $CuAl_{0.1}$ alloy (Fig. 7a) is larger than that of Cu (Fig. 2a), it indicates a change in the direction of the thermal gradient and compressive

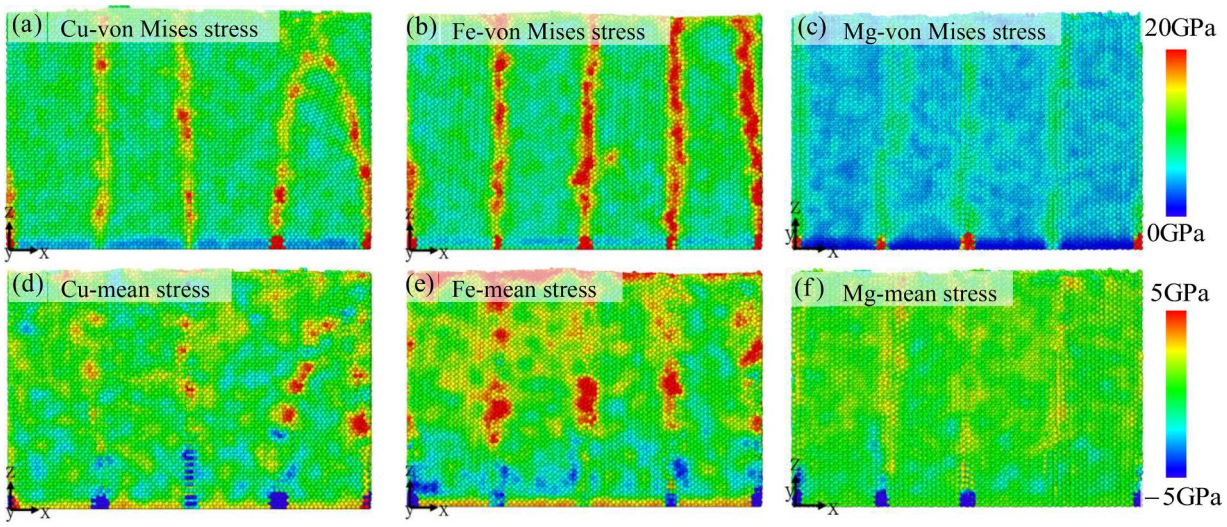

Fig. 6. The distribution of the residual stress expressed by the von Mises stress for (a) FCC Cu, (b) BCC Fe, (c) HCP Mg, where the range changes from 0 to 20 GPa; the mean stress for (d) FCC Cu, (e) BCC Fe, (f) HCP Mg, where the range changes from - 5 to 5 GPa.

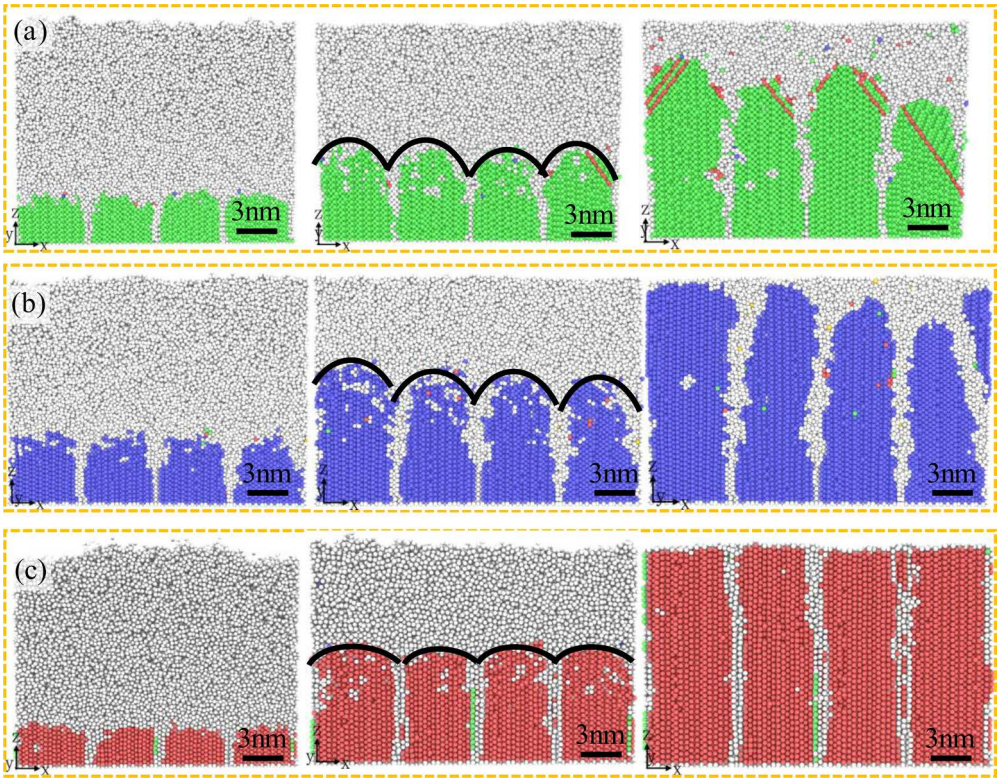

Fig. 7. The states of columnar crystal growth at the initial, middle, and final stages of solidification for $CuAl_{0.1}$ (a), $FeAl_{0.1}$ (b), and $MgAl_{0.1}$ (c). The black arcs represent the outline of the solidification front.

thermal stress. The alloying has a weak effect on the solid-liquid interface morphology of $FeAl_{0.1}$ and $MgAl_{0.1}$ alloys. Thus, the addition of a solute element would affect the wettability of the FCC phase (Zhao et al., 2019). When the molten pool is cooled to room temperature, the final structure shows the significant difference in the crystallization degree. A poor crystallinity is observed in the $CuAl_{0.1}$ alloy, and a large number of amorphous structures and discrete nucleation points exist at the top of the molten pool. The phenomenon is different from the pure Cu. The formation of amorphous phases depends on the competition between the cooling rate and the crystal growth rate (Zhong et al., 2014). The compressive thermal stress in the molten pool is not sufficient to save as the driving force for the formation of ordered bonds between atoms. The slight lateral epitaxial growth is presented in the $FeAl_{0.1}$ alloy at the later stage of solidification. The amorphous structure is formed at the competition between the lateral epitaxial growth and vertical growth, due to the low compressive thermal stress in the later stage of solidification and the high stacking fault energy of BCC structure. Thus, the crystallinity and grain morphology are worse than that of the pure metal Fe. However, the complete crystallization with the regular grain boundary is presented in the molten pool of the $MgAl_{0.1}$ alloy after solidification (Fig. 7c), forming a structure similar to that of the pure metal Mg (Fig. 2c). This result indicates that the evolution of thermal deformation/stress in HCP structure is similar before and after alloying. Therefore, the alloying effect of different crystal structures is different. Similarly, the dynamic solidification process of local atom is shown in the Fig. 8. The activity of atom in the liquid phase of HCP metals is higher than that in FCC and BCC metals. It suggests the faster atomic sinking and shorter time required to form a stable lattice structure in HCP metals. Meanwhile, the previous research points out that the lattice misfit caused by the atomic size difference between elements hinders the formation of the crystalline structure (Schuler and Rupert, 2017). Based on the characteristic of lattice structure and the calculation rule of lattice misfit (Li et al., 2020b; Senkov et al., 2011; Wang et al., 2018b), the addition of Al element in $CuAl_{0.1}$ alloy results in larger lattice mismatch, and exhibits the severe amorphization. $MgAl_{0.1}$ alloy has a small lattice mismatch and more complete crystal growth.

Fig. 9 shows the average growth rate of the solidification front, and reflects the difference of the dynamic solidification process in different alloys. For the CuAl0.1 alloy, there is an obvious fluctuation of the growth rate, which is relatively slow and generally lower than 0.02 nm/ps during the solidification process. Compared with the pure Cu (Fig. 4), there is no obvious acceleration process in the $CuAl_{0.1}$ alloy, due to the weak growth driving force induced by the compressive thermal stress (Wang et al., 2015). In addition, the change trend of growth rate in the $FeAl_{0.1}$ alloy is stable in the early stage and rapid in the later stage, consistent with that in the pure Fe. There is the obvious accelerated solidification stage in $MgAl_{0.1}$, which is consistent with that in Mg. Meanwhile, the average growth rate in the alloys is lower than that in the pure metal, resulting in a long time for columnar crystal growth in the molten pool. Among them, the phenomenon in $CuAl_{0.1}$ alloy shows more significant. Thus, this result proves that the lattice distortion induced by the solute addition reduces the driving force of solidification under certain solidification conditions (Sun et al., 2022; Wang et al., 2015).

The defect structures are exhibited in Fig. 10. A large number of stacking faults and twins are accumulated in the $CuAl_{0.1}$ alloy after

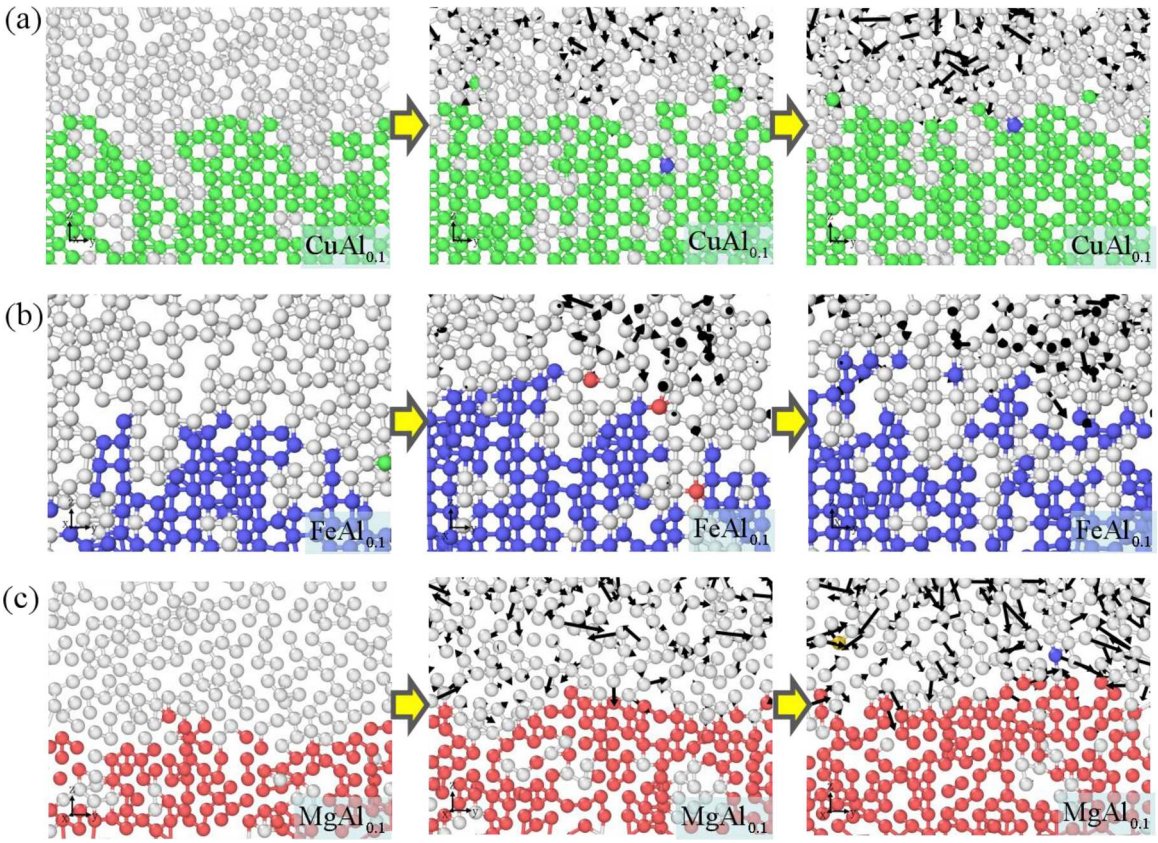

Fig. 8. Snapshot of local atomic motion during solidification process. (a) for $CuAl_{0.1}$, (b) for $FeAl_{0.1}$, and (c) for $MgAl_{0.1}$. The atomic colors are defined by CNA, where green atom denotes the FCC structure, blue atom represents the BCC structure, red atom is the HCP structure, and gray atom represents the liquid phase. The black arrow indicates the direction of atomic motion.

the molten pool is cooled. Due to the low stacking fault energy of the $CuAl_{0.1}$ alloy, the thermal stress deformation is dissipated during the solidification (Cai et al., 2022; Zhang et al., 2021a). The HCP clusters appear in the grain growth process in the BCC $FeAl_{0.1}$ alloy (Fig. 10(b)), owing to the alternating solid phase transformation under a complex thermal stress (Khodabakhshi et al., 2019). The grain boundaries formed in $CuAl_{0.1}$ and $FeAl_{0.1}$ alloys are more disordered than those in their pure metals. A few discrete vacancies are observed in the intragranular structure of $MgAl_{0.1}$ alloy. Thus, the alloying promotes the defects generation during the rapid solidification, consistent with previous research result (Haapalehto et al., 2022). The defects distribution further indicates that the alloying effect is weak in the HCP metal, compared with that in the FCC and BCC metals.

Fig. 11 shows the distribution of the von Mises stress and mean stress after molten pool cooling to room temperature. They are used to describe the residual stress caused by the repeated thermal expansion and contraction in the various alloys, and represents the thermal stress history of the molten pool. For the von Mises stress (Fig. 11a–c), the high stress is dispersed at the top of molten pool in the $CuAl_{0.1}$ due to the existence of a large number of amorphous phases. This result is different from the high stress zone located at the grain boundary in the pure Cu. Compared with the pure Fe, the high residual stress zone at the grain boundary becomes wider in the $FeAl_{0.1}$ alloy. Thus, the alloying coarsens the grain boundary. There are the low stresses in the HCP $MgAl_{0.1}$, this state is consistent with that in Mg. Similarly, for the mean stress, the low or negative stress is distributed in the grain interior of the three alloys. The residual stress generated by AM is inevitable, and presents the thermal history. Thus, the currently revealed stress distribution can serve as evidence for the formation mechanism of microcracks in AM materials. For example, the cracking mechanism varies from the intergranular thermal cracking in the FCC structure to the transgranular cold cracking in the BCC structure under severe residual stresses (Niu et al., 2023; Su et al., 2020).

The microstructure evolution during the AM process has been revealed through atomic simulation in the current work, but it should be noted that further experimental characterization of the real-time microstructure evolution is very advantageous for a deep understanding of the underlying mechanisms. However, the experimental methods to investigate the real-time microstructure evolution are still difficult at the atomic scale. Thus, an integrated multi-scale modeling and In-situ experimental approach need to be developed to assist in the microstructure regulation during AM process in the future work.

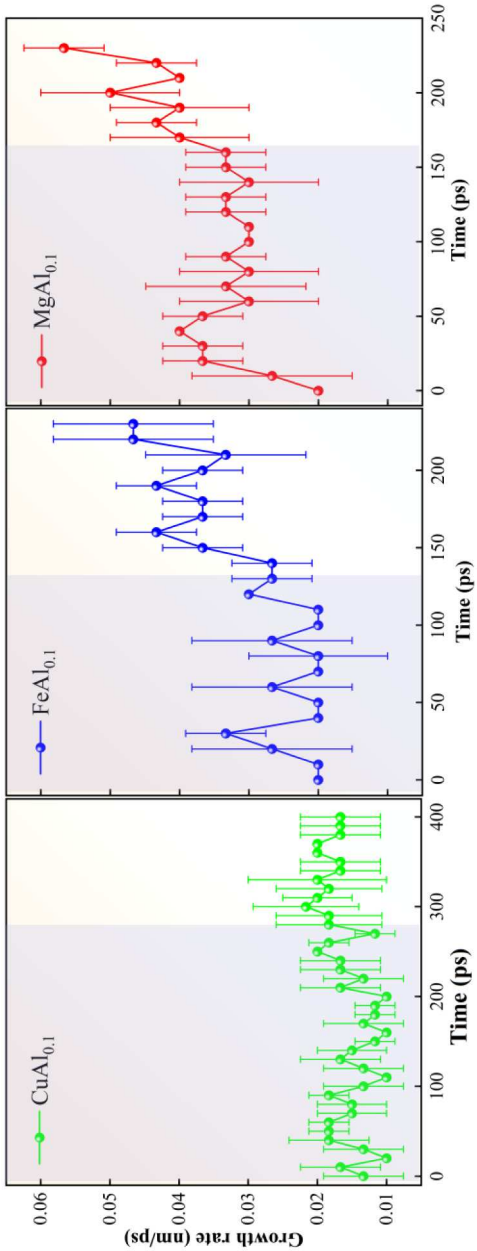

Fig. 9. The average growth rate of the solid-liquid interface of $CuAl_{0.1}$, $FeAl_{0.1}$, and $MgAl_{0.1}$.

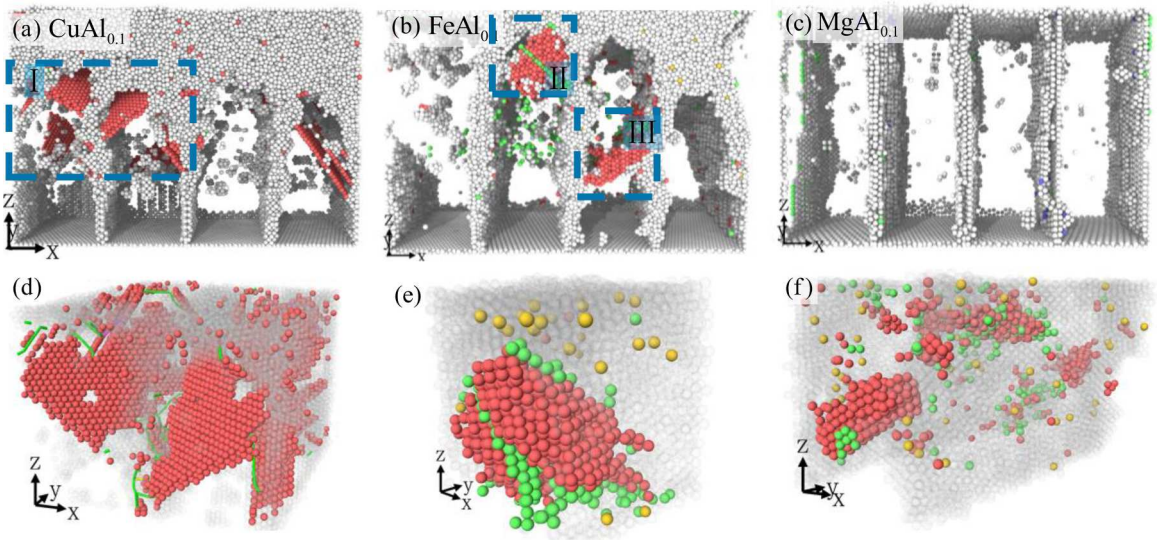

Fig. 10. The microstructure of defect in SLMed (a) CuAl0.1, (b) FeAl0.1, (c) MgAl0.1. The typical defects in region I, II, and III are highlighted in (d), (e) and (f).

4. Discussion

4.1. Heat flow and solute flow

The solidification deformation of a pure metal in molten pool is driven by the heat flow, while the solidification of the alloy involves both heat flow and solute flow. Therefore, the influence of the thermodynamic driving force and the chemical driving force on the non-equilibrium solidification during the AM process would be discussed. Fig. 12 exhibits the temperature distribution in FCC Cu, $CuAl_{0.1}$, BCC Fe, $FeAl_{0.1}$, and HCP Mg, $MgAl_{0.1}$. Obviously, the molten pool is divided into three regions (S, S-L and L) according to the temperature: the "S" region stands for the temperature lower than the melting point, the "S-L" region means the mixed high and low temperature, and the "L" region represents the temperature higher than the melting point. In the present work, the S, S-L and L regions are defined as the solid state, the solid-liquid mixed state, and the liquid state.

Meanwhile, the average temperature along the z-direction of the molten pool is counted (Fig. 13). The green shaded area describes the temperature of the solid-liquid mixing zone obtained from Fig. 12. There is an obvious distribution of the temperature gradient from the bottom to the top of the molten pool. For different crystal structures, the temperature gradient of the BCC Fe changes significantly, but that of the HCP Mg changes gently. However, the temperature distribution shows that the slope of the curve between the solidified zone and the liquid interface fluctuates slightly in the alloys. The temperature gradient of the solid-liquid mixing zone in the pure metal is greater than that in alloys. It gives a clear explanation for the long solidification time required in the alloys, and the complete formation of crystal structure in $CuAl_{0.1}$ and $FeAl_{0.1}$ due to the insufficient growth driving force. Meanwhile, the ratio of temperature gradient (G) to growth rate (R) is an important factor to affect the nucleation and growth. The value of G/R is small in HCP due to the high growth rate and low temperature gradient, and corresponds a relatively stable solid-liquid interface and strong growth ability (Li et al., 2020a, 2022).

Although the rapid solidification has a certain inhibiting effect on element segregation, the dynamic evolution of solute micro-segregation cannot be completely avoided in the alloys. It is closely related to the microstructure formation and mechanical property. In the previous work (Peng et al., 2023a, 2023b), the dynamic growth behavior of the FeCrNi medium-entropy alloy is simulated during the SLM process. It reveals the Cr segregation induced by the thermal process at the atomic scale, in agreement with the atom probe tomography characterization (Fu et al., 2022; Peng et al., 2023a, 2023b). The Cr microsegregation enhances the mechanical properties of FeCrNi alloys (Duan et al., 2022). The chemical-composition-induced driving force is an important factor in the solidification. Therefore, the quantitative analysis and accurate description for the dynamic evolution of elements are crucial.

According to the solute redistribution during the solidification, the composition in the pre-crystalline crystal and the amorphous phase is different. The heat and solute flows promote the combination of the heat and mass transfer under the non-equilibrium solidification conditions, and then affect the crystal morphology. There are a few solute atoms in the crystal, resulting in the solute concentration in the liquid phase (Fig. 14 (a, b)). In FCC $CuAl_{0.1}$ and BCC $FeAl_{0.1}$, the crystal has a weak ability to dissolve the solute compared with the liquid phase, consistent with the previous study (Liu et al., 2022b). Contrary to the extrusion of solute atoms into the liquid phase, more solute atoms accumulate in the solidification region at the rear of the molten pool in the HCP $MgAl_{0.1}$. The fluctuation of solute concentration modifies the solidification temperature of the liquid phase, resulting in the corresponding change in the supercooling (Oliveira et al., 2020). The redistribution characteristic of the solute atoms is closely related to the solidification state. According to the mixture rule (Shaikh et al., 2020), the melting point of $CuAl_{0.1}$ and $FeAl_{0.1}$ decrease due to the addition of the Al

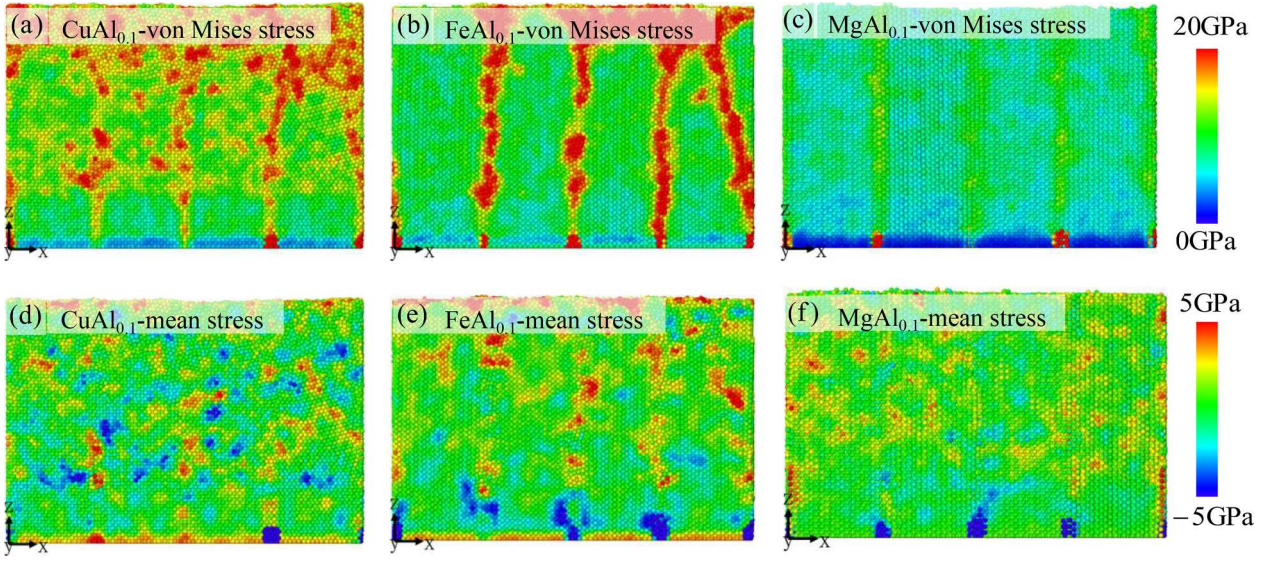

Fig. 11. The distribution of residual stress expressed by the von Mises stress for (a) FCC $CuAl_{0.1}$, (b) BCC $FeAl_{0.1}$, (c) HCP $MgAl_{0.1}$, where the range changes from 0 to 20 GPa; the mean stress for (d) FCC $CuAl_{0.1}$, (e) BCC $FeAl_{0.1}$, (f) HCP $MgAl_{0.1}$, where the range changes from −5 to 5 GPa.

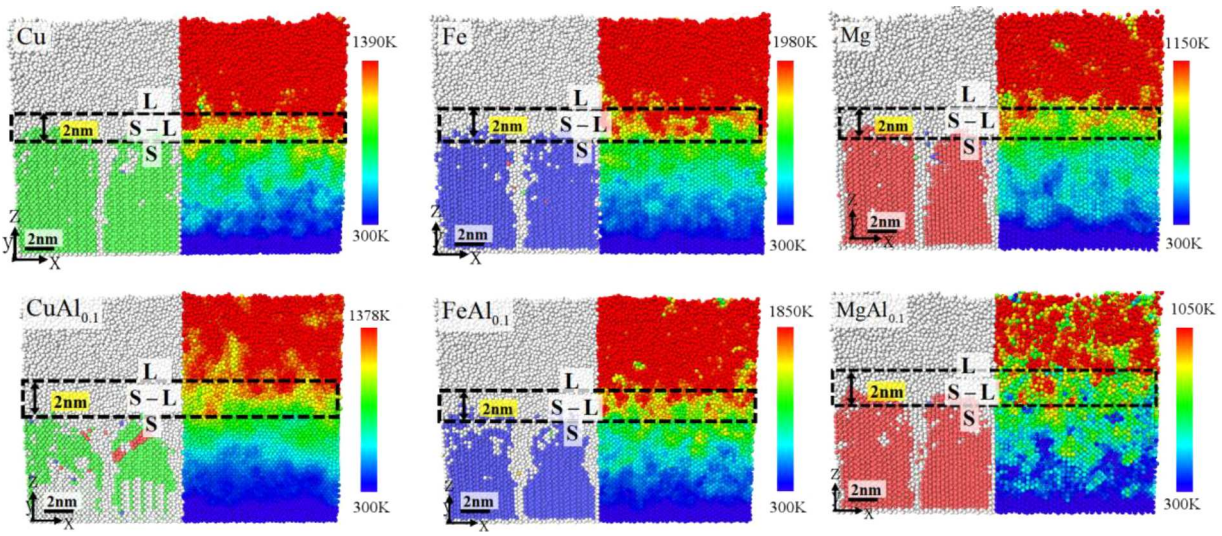

Fig. 12. The temperature distribution of the molten pool for FCC Cu, $CuAl_{0.1}$, BCC Fe, $FeAl_{0.1}$, and HCP Mg, and $MgAl_{0.1}$. Here, the atoms on the left and right sides of the molten pool are colored in different ways, respectively. For the atoms on the left, green atom denotes FCC structure, blue atom represents BCC structure, red atom is HCP structure, and gray atom is the liquid and grain boundary. For the atoms at right, atoms are colored based on temperature. The black dashed box has a height of 2 nm, and the upper and lower boundaries are 1 nm away from the front of the columnar crystal.

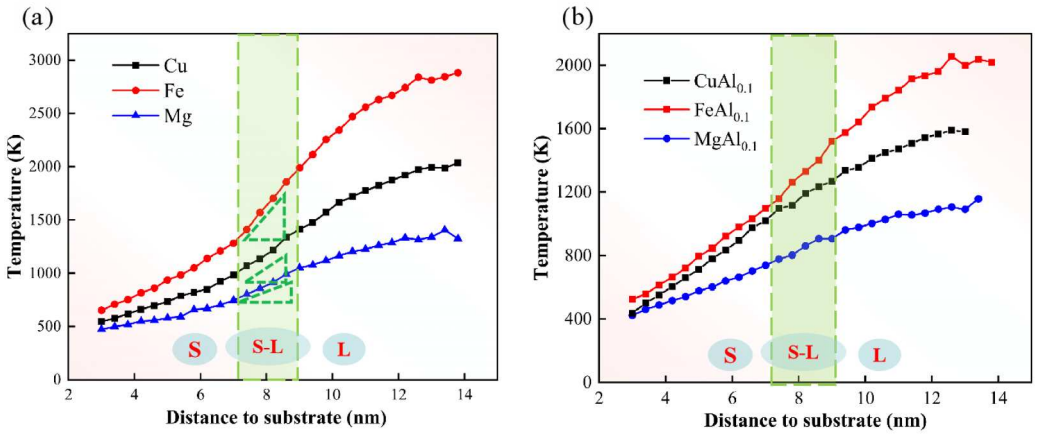

Fig. 13. Temperature distribution of molten pool along the growth direction for (a) pure metal, and (b) alloys. Here, S, S-L, and L are solid zone, solid-liquid mixing zone, and liquid zone.

element (Table 1). The Al atoms are expelled into the solid-liquid mixing zone and liquid phase due to the decrease of the Al solubility in the solid phase (Fig. 14). Thus, the local solidification temperature decreases at the solidification front and the supercooling increase, which is not conducive to the columnar growth. The mixture rule indicates that the Al addition hardly affects the melting point of $MgAl_{0.1}$, due to the melting point of Mg and Al element is very similar. Thus, for $MgAl_{0.1}$ alloy, the fluctuation of solute element between the solid and liquid phase has little effect on the solidification temperature. Among the three alloys, the small nucleation resistance and high nucleation ability of columnar crystal occur in $MgAl_{0.1}$. The constitutional supercooling caused by solute element can counteract the negative effect of high thermal gradient, which is always used as a strategy to limit the columnar crystal growth (Zhang et al., 2019a). Therefore, this analysis suggests that the dynamic fluctuation of the solute concentration controls the crystallization state.

4.2. *Crystal nucleation barriers energy*

According to the classical nucleation theory (Auer and Frenkel, 2001; Jafary-Zadeh et al., 2018; Shibuta and Suzuki, 2007), the heterogeneous nucleation is completed, and the total free energy changes to form the spherical coronal crystalline nucleus under the influence of the substrate. The nucleation barrier energy ΔG^* is maximum of the free energy change, which can be estimated from

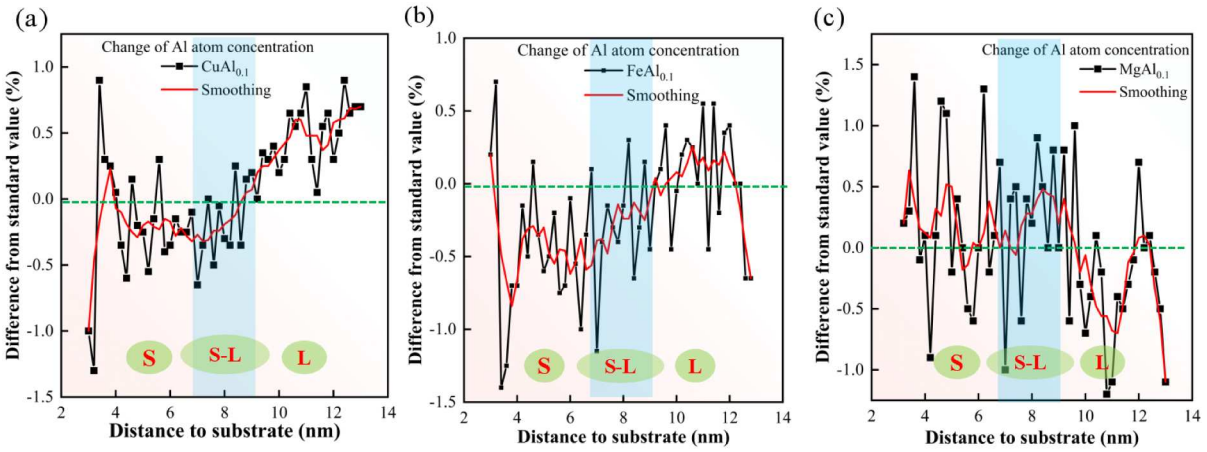

Fig. 14. Al atom concentration along the growth direction of the columnar crystal for (a) $CuAl_{0.1}$, (b) $FeAl_{0.1}$, and (c) $MgAl_{0.1}$, when the growth front is about 8 nm from the bottom of substrate. Here, S, S-L, and L are solid zone, solid-liquid mixing zone, and liquid zone.

critical nucleus size n^*(Yi et al., 2013).

$$n^* = 2\rho_n \frac{\Delta G^*}{\Delta G_v} \tag{3}$$

where ρ_n is the atomic number density of nucleation. ΔG_v is the difference of the free energy generated by the conversion of the liquid phase to solid phase per unit volume.

For materials with high supercooling, the crystallization driving force at the temperature, T^*, is expressed as:

$$\Delta G_v = \frac{\rho_n \Delta H_f T^* \Delta T}{T_m^2} \tag{4}$$

where ΔH_f is the latent heat per atom Shibuta and Suzuki, 2007), $\Delta T = T_m - T^*$ is supercooling, and T_m is the melting temperature, as shown in Table 1. Thus, combining Eqs. (3) and ((4), we can obtain:

$$n^* = \frac{2T_m^2}{\Delta H_f T^* \Delta T} \Delta G^* \tag{5}$$

where T^* is the critical phase transition temperature corresponding to the critical nucleus size. The related parameters are listed in Table 2.

In the present work, the multiple block regions with the same size in the molten pool are selected as the representative regions to investigate the energy change during the solidification process. Fig. 15(a–c) shows the average atomic potential energy in the region during the phase transformation process. Meanwhile, the variation in the number of solid phase atoms is described with the decrease of temperature (Fig. 15(d)), and shows a significant initial solidification point. It serves as the solidification critical state. At this time, the number of solidified atoms is regarded as the critical nucleation size, n^*, corresponding to a temperature of T^*. The statistical result is listed in Table 2.

A sharp decline phenomenon of the average potential energy is presented in Fig. 15(a-c). The temperature range for the sharp decrease of potential energy is 1279 - 1020 K in the pure Cu, and 1086 - 849 K in the $CuAl_{0.1}$ alloy; the temperature range is 1737 - 1425 K in the pure Fe, and 1596 - 1358 K in the $FeAl_{0.1}$ alloy; the temperature range is 924 - 808 K in the pure Mg and 801 - 709 K in the $MgAl_{0.1}$ alloy. The rapid potential energy change is consistent with the atom transition from the liquid phase to solid phase (Fig. 15d). In addition, the initial solidification temperature significantly decreases due to the alloying effect. It indicates a decrease in the supercooling. Among them, the supercooling of the HCP structure is similar before and after alloying. The FCC structured alloys have a

Table 2
Parameters for different crystallization metals.

	n*	T* (K)	ΔH_f (ev)	ΔT (K)
Cu	78	1279	0.15439	111
$CuAl_{0.1}$	59	1054	0.11923	324
Fe	51	1737	0.15381	243
$FeAl_{0.1}$	66	1533	0.12683	317
Mg	37	924	0.10807	226
$MgAl_{0.1}$	58	814	0.10415	236

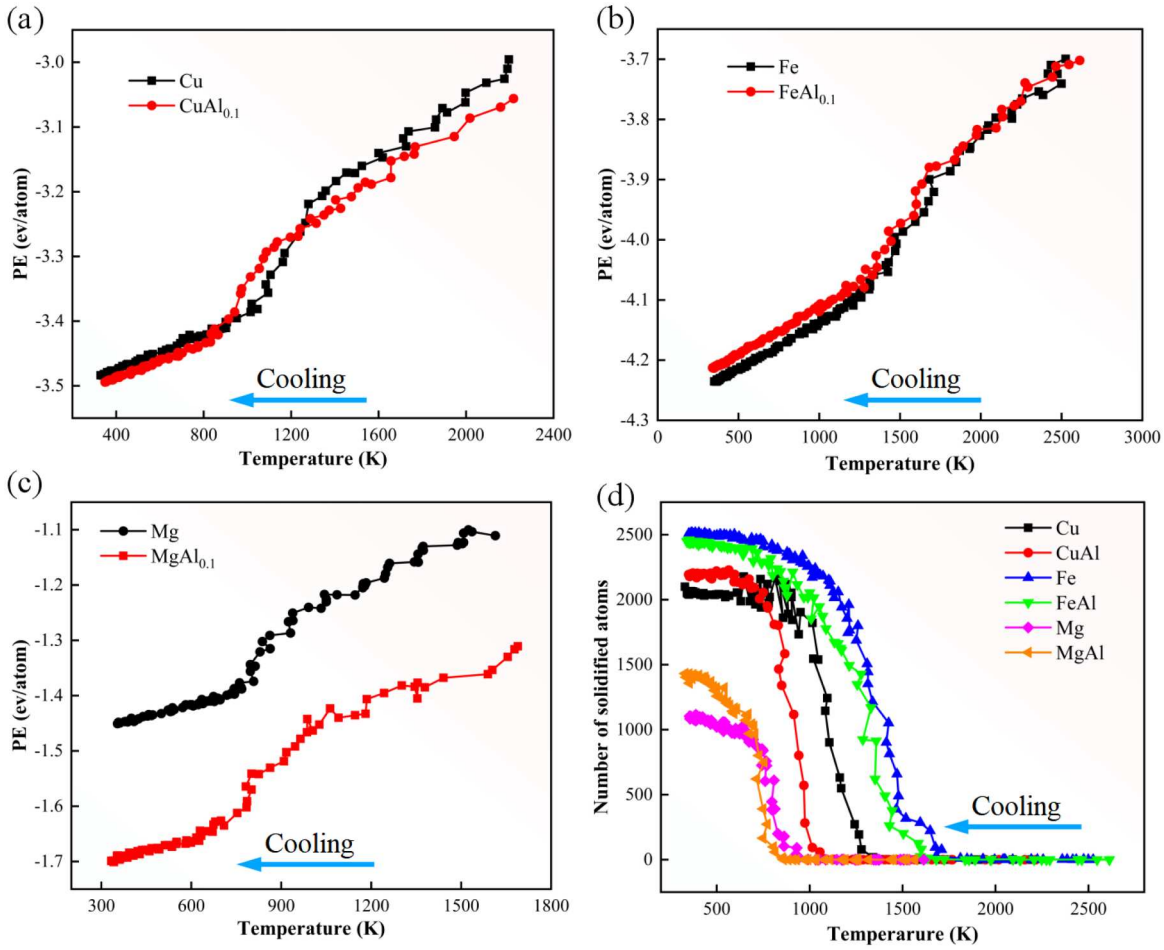

Fig. 15. The potential energy per atom during solidification in (a) FCC Cu, $CuAl_{0.1}$, (b) BCC Fe, $FeAl_{0.1}$, and (c) HCP Mg, $MgAl_{0.1}$. (d) The number of solidified atoms.

significant decrease in supercooling compared to the pure metals. Meanwhile, the alloying reduces the solidification temperature range.

Fig. 16 shows the evolution of average atomic potential energy during the solidification of the single crystal cell. The atoms of the crystal cell solidify from a disordered structure to an ordered structure due to the high temperature gradient and supercooling. When the stable bonds are formed between the atoms, there is a significant mutation in the potential energy in Cu, Fe, and Mg. However, the potential energy decreases smoothly after alloying.

Based on the statistical results of Figs. 15–16 and Eqs. (3–5), the nucleation barriers energy for FCC Cu, $CuAl_{0.1}$, BCC Fe, $FeAl_{0.1}$, and HCP Mg, $MgAl_{0.1}$ is calculated as shown in Fig. 17. When the complexity of composition element is similar, there is a larger nucleation barrier in the FCC metals and the small nucleation barrier in the HCP metals. This trend is obtained in other high concentration alloys (Jafary-Zadeh et al., 2018). The nucleation barrier energy of the BCC CoFeNiPd alloy is significantly lower than that of the FCC CoFeNiPd alloy when the seeds of different crystal structures are preset (Jafary-Zadeh et al., 2018). The alloying would increase the nucleation barrier, and makes the nucleation and growth more difficult, agreeing with the result described in Fig. 7. However, a larger nucleation barrier energy appears in high concentration alloys. The current results explain the differences in the average growth rates of the metals with various crystal structures. When the complexity of the constituent elements of the metal is similar, the HCP structure with a low nucleation barrier energy exhibits high average growth rates, while the average growth rate is the smallest in FCC structure (Fig. 4 and 9). Thus, the regulation of phase formation could be a route to achieve the specific microstructures and properties of the AM materials.

5. Conclusion

In this study, the rapid thermal deformation process of the AM pure metals and alloys with different crystal structures, including FCC Cu, $CuAl_{0.1}$, BCC Fe, $FeAl_{0.1}$, and HCP Mg, $MgAl_{0.1}$ is investigated by the large-scale atomic simulation combined with the nucleation theory.

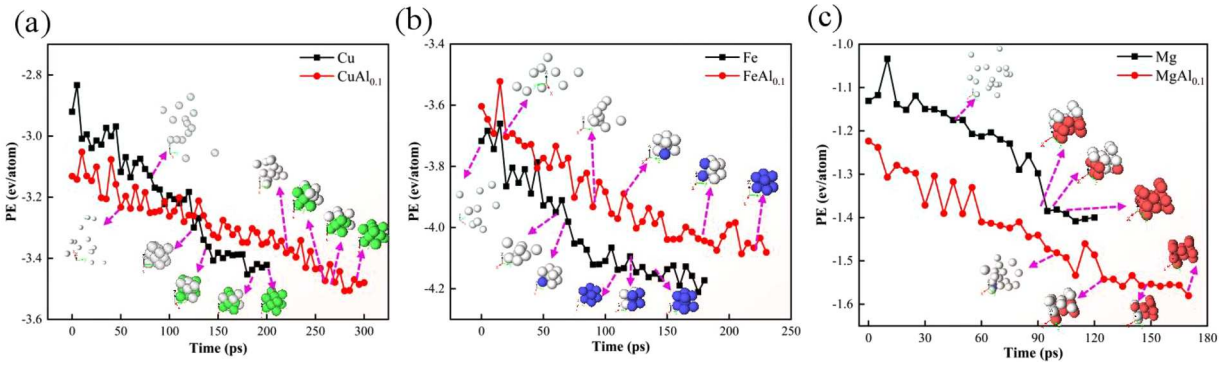

Fig. 16. The evolution of potential energy during the single crystal cell solidification process.

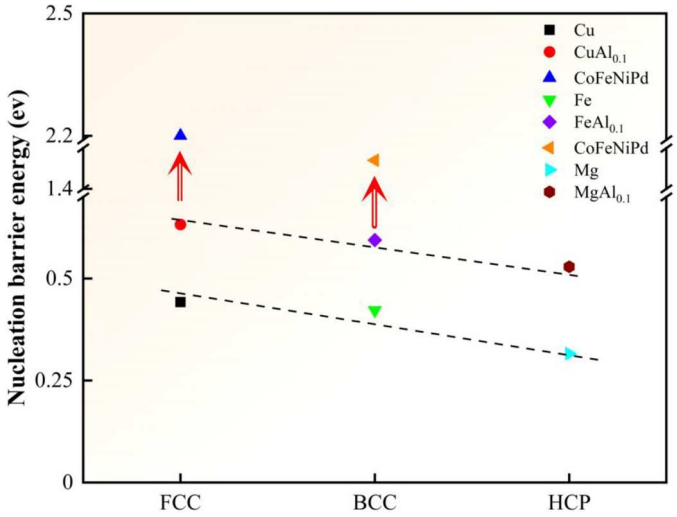

Fig. 17. The nucleation barrier free energy for FCC Cu, $CuAl_{0.1}$, BCC Fe, $FeAl_{0.1}$, HCP Mg, $MgAl_{0.1}$ metals, and the CoFeNiPd alloy with FCC or BCC structure (Jafary-Zadeh et al., 2018).

The dynamic columnar crystal growth and the microstructure evolution within grains are observed at the nanoscale in the pure metals during the later solidification stage. The local stress concentration caused by the liquid-to-solid phase transition drives the formation of stacking faults and twinning in the competitive growth area. The critical radius of spherical coronal nucleus in the solidification front of the FCC and BCC structures is larger than that of the HCP structure owing to the repeated thermal stress and the capillary effect. In addition, the high residual stress occurs in the grain boundary when the melt pool is cooled to room temperature, and the low residual stress takes place in the HCP and FCC structures compared with the BCC structure.

Under the same cooling strategy, the introduction of the Al atom significantly weakens the solidification driving force of the molten pool in the corresponding structured alloy. The solute Al atoms segregate towards a liquid phase in the $CuAl_{0.1}$ and $FeAl_{0.1}$ alloys during solidification, which is contrary to $MgAl_{0.1}$. The chemical driving force caused by the solute redistribution is coupled with the thermal driving force generated by the thermal gradient, resulting in the significant morphological difference.

According to the classical nucleation theory, when the complexity of composition element is similar, there is the high nucleation barrier energy in metals with the FCC structure, compared to the BCC and HCP structure. This trend corresponds to the weak crystallization capacity and grain growth rate of FCC metals. On the contrast, the HCP metals show the superior nucleation ability and growth rate.

The current work not only deeply reveals the intrinsic physical mechanism of thermal deformation induced crystallization and microstructure formation considering the influence of the crystal structure as well as the alloying, but also provides a theoretical guidance to design the AM metals with the outstanding performance. Furthermore, it is worthwhile highlighting that an integrated multiscale modeling and In-situ experimental approach can enable a full-field real-time microstructure evolution in future work.

CRediT authorship contribution statement

Jing Peng: Formal analysis, Software, Investigation, Data curation, Writing – original draft. **Jia Li:** Conceptualization,

Methodology, Validation, Writing – review & editing, Supervision, Funding acquisition. **Bin Liu:** Conceptualization, Validation, Supervision. **Qihong Fang:** Conceptualization, Validation, Writing – review & editing, Supervision, Funding acquisition. **Peter K Liaw:** Writing – review & editing, Project administration, Supervision, Funding acquisition.

Declaration of Competing Interest

The authors declare that they have no known competing financial interests or personal relationships that could have appeared to influence the work reported in this paper.

Data availability

Data will be made available on request.

Acknowledgments

This work was supported by the National Natural Science Foundation of China (U2267252, 12172123, and 12072109), Natural Science Foundation of Hunan Province (2022JJ20001), and the Hunan Provincial Innovation Foundation For Postgraduate (CX20220378). PKL very much appreciates the support from (1) the National Science Foundation (DMR - 1611180, 1809640, and 2226508) and (2) the US Army Research Office (W911NF-13-1-0438 and W911NF-19-2-0049).

Supplementary materials

Supplementary material associated with this article can be found, in the online version, at doi:10.1016/j.ijplas.2023.103831.

References

An, Y., Xu, X., Hao, Y., Dong, R., Hou, H., Zhao, Y., Gu, T., Wang, H., 2022. Effect of Co addition on solidification velocity, hardness and refined structure transformation mechanisms of undercooled Ni-Cu-Co alloys. J. Alloy. Compd. 921, 166150.
Auer, S., Frenkel, D., 2001. Suppression of crystal nucleation in polydisperse colloids due to increase of the surface free energy. Nature 413, 711–713.
Balbaa, M., Mekhiel, S., Elbestawi, M., McIsaac, J., 2020. On selective laser melting of Inconel 718: densification, surface roughness, and residual stresses. Mater. Design 193, 108818.
Bandyopadhyay, A., Traxel, K.D., Lang, M., Juhasz, M., Eliaz, N., Bose, S., 2022. Alloy design via additive manufacturing: advantages, challenges, applications and perspectives. Mater. Today 52, 207–224.
Blakey-Milner, B., Gradl, P., Snedden, G., Brooks, M., Pitot, J., Lopez, E., Leary, M., Berto, F., Du Plessis, A., 2021. Metal additive manufacturing in aerospace: a review. Mater. Design 209, 110008.
Cai, X., Wang, Z., Dong, L., Yang, M., Zhou, J., Xue, F., 2022. Advanced mechanical properties of nickel-aluminum bronze/steel composite structure prepared by wire-arc additive manufacturing. Mater. Design 221, 110969.
Chen, F., Yan, W., 2020. High-fidelity modelling of thermal stress for additive manufacturing by linking thermal-fluid and mechanical models. Mater. Design 196, 109185.
Chew, Y., Bi, G., Zhu, Z., Ng, F., Weng, F., Liu, S., Nai, S., Lee, B., 2019. Microstructure and enhanced strength of laser aided additive manufactured CoCrFeNiMn high entropy alloy. Mater. Sci. Eng. A 744, 137–144.
Chung, D., Lee, J., He, Q., Kim, Y., Lim, K., Kim, H., Yang, Y., Na, Y., 2023. Hetero-deformation promoted strengthening and toughening in BCC rich eutectic and near eutectic high entropy alloys. J. Mater. Sci. Technol. 146, 1–9.
Dai, R., Neuefeind, J.C., Quirinale, D.G., Kelton, K.F., 2020. X-ray and neutron scattering measurements of ordering in a Cu46Zr54 liquid. J. Chem. Phys. 152.
DebRoy, T., Mukherjee, T., Milewski, J.O., Elmer, J.W., Ribic, B., Blecher, J.J., Zhang, W., 2019. Scientific, technological and economic issues in metal printing and their solutions. Nat. Mater. 18 (10), 1026–1032.
DebRoy, T., Wei, H.L., Zuback, J.S., Mukherjee, T., Elmer, J.W., Milewski, J.O., Beese, A.M., Wilson-Heid, A., Zhang, W., 2018. Additive manufacturing of metallic components–process, structure and properties. Prog. Mater. Sci. 92, 112–224.
Dickel, D.E., Baskes, M.I., Aslam, I., Barrett, C.D., 2018. New interatomic potential for Mg–Al–Zn alloys with specific application to dilute Mg-based alloys. Model. Simul. Mater. Sci. Eng. 26, 045010.
Duan, H., Liu, B., Fu, A., He, J., Yang, T., Liu, C.T., Liu, Y., 2022. Segregation enabled outstanding combination of mechanical and corrosion properties in a FeCrNi medium entropy alloy manufactured by selective laser melting. J. Mater. Sci. Technol. 99, 207–214.
Fu, A., Liu, B., Li, Z., Wang, B., Cao, Y., Liu, Y., 2022. Dynamic deformation behavior of a FeCrNi medium entropy alloy. J. Mater. Sci. Technol. 100, 120–128.
Fu, Y., Guo, N., Wang, G., Yu, M., Cheng, Q., Zhang, D., 2021. Underwater additive manufacturing of Ti-6Al-4V alloy by laser metal deposition: formability, gran growth and microstructure evolution. Mater. Design 197, 109196.
Fujieda, T., Chen, M., Shiratori, H., Kuwabara, K., Yamanaka, K., Koizumi, Y., Chiba, A., Watanabe, S., 2019. Mechanical and corrosion properties of CoCrFeNiTi-based high-entropy alloy additive manufactured using selective laser melting. Add. Manuf. 25, 412–420.
Gao, Z., Jie, W., Liu, Y., Zheng, Y., Luo, H., 2019. A model for coupling prediction of inverse segregation and porosity for up-vertical unidirectional solidification of Al–Cu alloys. J. Alloy. Compd. 797, 514–522.
Ghoncheh, M., Sanjari, M., Cyr, E., Kelly, J., Pirgazi, H., Shakerin, S., Hadadzadeh, A., Amirkhiz, B.S., Kestens, L., Mohammadi, M., 2020. On the solidification characteristics, deformation, and functionally graded interfaces in additively manufactured hybrid aluminum alloys. Int. J. Plast. 133, 102840.
Ghorbanpour, S., Deshmukh, K., Sahu, S., Riemslag, T., Reinton, E., Borisov, E., Popovich, A., Bertolo, V., Jiang, Q., Sanchez, M.T., 2022. Additive manufacturing of functionally graded inconel 718: effect of heat treatment and building orientation on microstructure and fatigue behaviour. J. Mater. Process. Technol. 306, 117573.
Gong, G., Ye, J., Chi, Y., Zhao, Z., Wang, Z., Xia, G., Du, X., Tian, H., Yu, H., Chen, C., 2021. Research status of laser additive manufacturing for metal: a review. J. Mater. Res. Technol. 15, 855–884.

Guo, C., Li, G., Li, S., Hu, X., Lu, H., Li, X., Xu, Z., Chen, Y., Li, Q., Lu, J., 2023. Additive manufacturing of Ni-based superalloys: residual stress, mechanisms of crack formation and strategies for crack inhibition. Nano Mater. Sci. 5, 53–77.
Haapalehto, M., Pinomaa, T., Wang, L., Laukkanen, A., 2022. An atomistic simulation study of rapid solidification kinetics and crystal defects in dilute Al–Cu alloys. Comput. Mater. Sci. 209, 111356.
Hashemi, S.M., Parvizi, S., Baghbanijavid, H., Tan, A.T., Nematollahi, M., Ramazani, A., Fang, N.X., Elahinia, M., 2022. Computational modelling of process–structure–property–performance relationships in metal additive manufacturing: a review. Int. Mater. Rev. 67, 1–46.
Hu, D., Grilli, N., Wang, L., Yang, M., Yan, W., 2022. Microscale residual stresses in additively manufactured stainless steel: computational simulation. J. Mech. Phys. Solids 161, 104822.
Huang, Y., Fleming, T.G., Clark, S.J., Marussi, S., Fezzaa, K., Thiyagalingam, J., Leung, C.L.A., Lee, P.D., 2022. Keyhole fluctuation and pore formation mechanisms during laser powder bed fusion additive manufacturing. Nat. Commun. 13, 1170.
Jafary-Zadeh, M., Aitken, Z.H., Tavakoli, R., Zhang, Y.W., 2018. On the controllability of phase formation in rapid solidification of high entropy alloys. J. Alloy. Compd. 748, 679–686.
Ji, K., Dorari, E., Clarke, A.J., Karma, A., 2023. Microstructural pattern formation during far-from-equilibrium alloy solidification. Phys. Rev. Lett. 130, 026203.
Jiang, C., Mo, Y., Wang, H., Li, R., Huang, M., Jiang, S., 2021. Molecular dynamics simulation of the production of hollow silver nanoparticles under ultrafast laser irradiation. Comput. Mater. Sci. 196, 110545.
Jiang, Q., Liu, H., Li, J., Yang, D., Zhang, Y., Yang, W., 2020. Atomic-level understanding of crystallization in the selective laser melting of Fe50Ni50 amorphous alloy. Addit. Manuf. 34, 101369.
Joshi, S.S., Keller, C., Mas, L., Lefebvre, W., Hug, E., Couzinie, J.P., 2023. On the origin of the strain hardening mechanisms of Ni20Cr alloy manufactured by laser powder bed fusion. Int. J. Plast. 165, 103610.
Kaptay, G., 2012. On the order–disorder surface phase transition and critical temperature of pure metals originating from BCC, FCC, and HCP crystal structures. Int. J. Thermophys. 33, 1177–1190.
Kashchiev, D., 2000. Nucleation. Elsevier.
Keller, T., Lindwall, G., Ghosh, S., Ma, L., Lane, B.M., Zhang, F., Kattner, U.R., Lass, E.A., Heigel, J.C., Idell, Y., 2017. Application of finite element, phase-field, and CALPHAD-based methods to additive manufacturing of Ni-based superalloys. Acta Mater 139, 244–253.
Khodabakhshi, F., Farshidianfar, M., Bakhshivash, S., Gerlich, A., Khajepour, A., 2019. Dissimilar metals deposition by directed energy based on powder-fed laser additive manufacturing. J. Manuf. Process. 43, 83–97.
Khodabakhshi, F., Farshidianfar, M., Gerlich, A., Nosko, M., Trembošová, V., Khajepour, A., 2020. Effects of laser additive manufacturing on microstructure and crystallographic texture of austenitic and martensitic stainless steels. Addit. Manuf. 31, 100915.
Kurian, S., Mirzaeifar, R., 2020. Selective laser melting of aluminum nano-powder particles, a molecular dynamics study. Addit. Manuf. 35, 101272.
Leung, C.L.A., Marussi, S., Atwood, R.C., Towrie, M., Withers, P.J., Lee, P.D., 2018. In situ X-ray imaging of defect and molten pool dynamics in laser additive manufacturing. Nat. Commun. 9, 1355.
Li, J., Yi, M., Wu, H., Fang, Q., Liu, Y., Liu, B., Zhou, K., Liaw, P.K., 2020a. Fine-grain-embedded dislocation-cell structures for high strength and ductility in additively manufactured steels. Mater. Sci. Eng. A 790, 139736.
Li, L., Fang, Q., Li, J., Liu, B., Liu, Y., Liaw, P.K., 2020b. Lattice-distortion dependent yield strength in high entropy alloys. Mater. Sci. Eng. A 784, 139323.
Li, R., Niu, P., Yuan, T., Li, Z., 2021a. Displacive transformation as pathway to prevent micro-cracks induced by thermal stress in additively manufactured strong and ductile high-entropy alloys. T. Nonferr. Metal. Soc. 31, 1059–1073.
Li, S., Li, J., Jiang, Z., Cheng, Y., Li, Y., Tang, S., Leng, J., Chen, H., Zou, Y., Zhao, Y., 2022. Controlling the columnar-to-equiaxed transition during directed energy deposition of Inconel 625. Addit. Manuf. 57, 102958.
Li, X., Wang, X., Saunders, M., Suvorova, A., Zhang, L., Liu, Y., Fang, M., Huang, Z., Sercombe, T.B., 2015. A selective laser melting and solution heat treatment refined Al–12Si alloy with a controllable ultrafine eutectic microstructure and 25% tensile ductility. Acta Mater. 95, 74–82.
Li, X., Yi, D., Liu, B., Zhang, J., Yang, X., Wang, C., Feng, Y., Bai, P., Liu, Y., Qian, M., 2020c. Graphene-strengthened Inconel 625 alloy fabricated by selective laser melting. Mater. Sci. Eng. A 798, 140099.
Li, Z., Cui, Y., Yan, W., Zhang, D., Fang, Y., Chen, Y., Yu, Q., Wang, G., Ouyang, H., Fan, C., 2021b. Enhanced strengthening and hardening via self-stabilized dislocation network in additively manufactured metals. Mater. Today 50, 79–88.
Li, Z., Li, Z., Tan, Z., Xiong, D.B., Guo, Q., 2020d. Stress relaxation and the cellular structure-dependence of plastic deformation in additively manufactured AlSi10Mg alloys. Int. J. Plast. 127, 102640.
Liu, F., Xie, H., He, W., 2022a. Multi-field coupling fatigue behavior of laser additively manufactured metallic materials: a review. J. Mater. Res. Technol. 22, 2819–2843.
Liu, P., Wang, Z., Xiao, Y., Lebensohn, R.A., Liu, Y., Horstemeyer, M.F., Cui, X., Chen, L., 2020. Integration of phase-field model and crystal plasticity for the prediction of process-structure-property relation of additively manufactured metallic materials. Int. J. Plast. 128, 102670.
Liu, Z., Zhao, D., Wang, P., Yan, M., Yang, C., Chen, Z., Lu, J., Lu, Z., 2022b. Additive manufacturing of metals: microstructure evolution and multistage control. J. Mater. Sci. Technol. 100, 224–236.
Lu, H., Deng, W., Luo, K., Chen, Y., Wang, J., Lu, J., 2023. Tailoring microstructure of additively manufactured Ti6Al4V titanium alloy using hybrid additive manufacturing technology. Addit. Manuf. 63, 103416.
Lv, Y., Lang, X., Su, C., Cao, L., Wang, L., 2022. Stacking fault and nano-twins dominating strengthening mechanism of (CuZnMnNi) 100-xSnx high entropy brass alloy prepared by mechanical alloying and fast hot pressing sintering. Mater. Lett. 312, 131614.
Mahata, A., Mukhopadhyay, T., Zaeem, M.A., 2022a. Liquid ordering induced heterogeneities in homogeneous nucleation during solidification of pure metals. J. Mater. Sci. Technol. 106, 77–89.
Mahata, A., Mukhopadhyay, T., Zaeem, M.A., 2022b. Modified embedded-atom method interatomic potentials for Al-Cu, Al-Fe and Al-Ni binary alloys: from room temperature to melting point. Comput. Mater. Sci. 201, 110902.
Martin, A.A., Calta, N.P., Hammons, J.A., Khairallah, S.A., Nielsen, M.H., Shuttlesworth, R.M., Sinclair, N., Matthews, M.J., Jeffries, J.R., Willey, T.M., 2019. Ultrafast dynamics of laser-metal interactions in additive manufacturing alloys captured by in situ X-ray imaging. Mater. Today Adv. 1, 100002.
Martin, J.H., Yahata, B., Mayer, J., Mone, R., Stonkevitch, E., Miller, J., Mark, R., Schaedler, T., Hundley, J., Callahan, P., 2020. Grain refinement mechanisms in additively manufactured nano-functionalized aluminum. Acta Mater 200, 1022–1037.
McKeown, J.T., Kulovits, A.K., Liu, C., Zweiacker, K., Reed, B.W., LaGrange, T., Wiezorek, J.M., Campbell, G.H., 2014. In situ transmission electron microscopy of crystal growth-mode transitions during rapid solidification of a hypoeutectic Al–Cu alloy. Acta Mater 65, 56–68.
McLouth, T.D., Witkin, D.B., Bean, G.E., Sitzman, S.D., Adams, P.M., Lohser, J.R., Yang, J.M., Zaldivar, R.J., 2020. Variations in ambient and elevated temperature mechanical behavior of IN718 manufactured by selective laser melting via process parameter control. Mater. Sci. Eng. A 780, 139184.
Niu, P., Li, R., Fan, Z., Cao, P., Zheng, D., Wang, M., Deng, C., Yuan, T., 2023. Inhibiting cracking and improving strength for additive manufactured AlxCoCrFeNi high entropy alloy via changing crystal structure from BCC-to-FCC. Addit. Manuf. 71, 103584.
Oliveira, J.P., LaLonde, A., Ma, J., 2020. Processing parameters in laser powder bed fusion metal additive manufacturing. Mater. Design 193, 108762.
Papanikolaou, M., Rodriguez-Hernandez, F., Jolly, M., Salonitis, K., 2022. Effects of crystallinity on residual stresses via molecular dynamics simulations. Phys. Rev. E 106, 045302.
Peng, J., Li, J., Liu, B., Wang, J., Chen, H., Feng, H., Zeng, X., Duan, H., Cao, Y., He, J., 2023a. Formation process and mechanical properties in selective laser melted multi-principal-element alloys. J. Mater. Sci. Technol. 133, 12–22.
Peng, J., Liu, B., Li, W., Liaw, P.K., Li, J., Fang, Q., 2023b. Data-driven investigation of microstructure and surface integrity in additively manufactured multi-principal-element alloys. J. Alloy. Compd. 937, 168431.
Picard, E.A., Sansoz, F., 2022. Ni solute segregation and associated plastic deformation mechanisms into random FCC Ag, BCC Nb and HCP Zr polycrystals. Acta Mater 240, 118367.

Plimpton, S., 1995. Fast parallel algorithms for short-range molecular dynamics. J. Comput. Phys. 117, 1–19.
Porter, D.A., Easterling, K.E., Sherif, M.Y., 2021. Phase Transformations in Metals and Alloys. CRC press.
Raghavan, N., Dehoff, R., Pannala, S., Simunovic, S., Kirka, M., Turner, J., Carlson, N., Babu, S.S., 2016. Numerical modeling of heat-transfer and the influence of process parameters on tailoring the grain morphology of IN718 in electron beam additive manufacturing. Acta Mater 112, 303–314.
Ren, J., Zhang, Y., Zhao, D., Chen, Y., Guan, S., Liu, Y., Liu, L., Peng, S., Kong, F., Poplawsky, J.D., 2022. Strong yet ductile nanolamellar high-entropy alloys by additive manufacturing. Nature 608, 62–68.
Richter, J., Bartzsch, G., Scherbring, S., Bolender, A., Vollmer, M., Mola, J., Volkova, O., Niendorf, T., 2022. Metastable CrMnNi steels processed by laser powder bed fusion: experimental assessment of elementary mechanisms contributing to microstructure, properties and residual stress. Sci. Rep. 12, 21862.
Schuler, J.D., Rupert, T.J., 2017. Materials selection rules for amorphous complexion formation in binary metallic alloys. Acta Mater 140, 196–205.
Senkov, O., Scott, J., Senkova, S., Miracle, D., Woodward, C., 2011. Microstructure and room temperature properties of a high-entropy TaNbHfZrTi alloy. J. Alloy. Compd. 509, 6043–6048.
Senkov, O., Wilks, G., Miracle, D., Chuang, C., Liaw, P., 2010. Refractory high-entropy alloys. Intermetallics 18, 1758–1765.
Shaikh, S.M., Hariharan, V., Yadav, S.K., Murty, B., 2020. CALPHAD and rule-of-mixtures: a comparative study for refractory high entropy alloys. Intermetallics 127, 106926.
Shibuta, Y., Suzuki, T., 2007. Melting and nucleation of iron nanoparticles: a molecular dynamics study. Chem. Phys. Lett. 445, 265–270.
Song, B., Yu, T., Jiang, X., Xi, W., Lin, X., 2021. Development mechanism and solidification morphology of molten pool generated by laser cladding. Int. J. Therm. Sci. 159, 106579.
Stukowski, A., 2009. Visualization and analysis of atomistic simulation data with OVITO–the open visualization tool. Model. Simul. Mater. Sci. Eng. 18, 015012.
Stukowski, A., Albe, K., 2010. Extracting dislocations and non-dislocation crystal defects from atomistic simulation data. Model. Simul. Mater. Sci. Eng 18, 085001.
Su, Y., Luo, S., Wang, Z., 2020. Microstructure evolution and cracking behaviors of additively manufactured AlxCrCuFeNi2 high entropy alloys via selective laser melting. J. Alloy. Compd. 842, 155823.
Sui, S., Chew, Y., Hao, Z., Weng, F., Tan, C., Du, Z., Bi, G., 2022. Effect of cyclic heat treatment on microstructure and mechanical properties of laser aided additive manufacturing Ti–6Al–2Sn–4Zr–2Mo alloy. Adv. Powder Mater. 1, 100002.
Sun, Z., Ma, Y., Ponge, D., Zaefferer, S., Jägle, E.A., Gault, B., Rollett, A.D., Raabe, D., 2022. Thermodynamics-guided alloy and process design for additive manufacturing. Nat. Commun. 13, 4361.
Tan, Q., Yin, Y., Prasad, A., Li, G., Zhu, Q., StJohn, D.H., Zhang, M.X., 2022. Demonstrating the roles of solute and nucleant in grain refinement of additively manufactured aluminium alloys. Addit. Manuf. 49, 102516.
Tang, Y.T., Panwisawas, C., Ghoussoub, J.N., Gong, Y., Clark, J.W., Németh, A.A., McCartney, D.G., Reed, R.C., 2021. Alloys-by-design: application to new superalloys for additive manufacturing. Acta Mater 202, 417–436.
Tsuzuki, H., Branicio, P.S., Rino, J.P., 2007. Structural characterization of deformed crystals by analysis of common atomic neighborhood. Comput. Phys. Commun. 177, 518–523.
Valencia, J.J., Quested, P., 2001. Thermophysical Properties. Modeling for casting and solidification processing, p. 189.
Varillas, J., Očenášek, J., Torner, J., Alcalá, J., 2021. Understanding imprint formation, plastic instabilities and hardness evolutions in FCC, BCC and HCP metal surfaces. Acta Mater 217, 117122.
Wang, F., Liu, Z.L., Qiu, D., Taylor, J.A., Easton, M.A., Zhang, M.X., 2015. The influence of the effect of solute on the thermodynamic driving force on grain refinement of Al alloys. Metall. Mater. Trans. A 46, 505–515.
Wang, G., Zhang, Y., Zou, B., Liu, Y., Zheng, S., Li, X., Yan, W., Li, Z., Wang, Y.M., 2023a. Enhanced plasticity due to melt pool flow induced uniform dispersion of reinforcing particles in additively manufactured metallic composites. Int. J. Plast. 164, 103591.
Wang, W., Luo, T., Liu, Z., Luo, S., Zhu, M., 2023b. Influences of cooling rate on solidification microstructure and carbide of GCr15 bearing steel. Metall. Mater. Trans. B 54, 776–792.
Wang, W., Yung, K., Choy, H., Xiao, T., Cai, Z., 2018a. Effects of laser polishing on surface microstructure and corrosion resistance of additive manufactured CoCr alloys. Appl. Surf. Sci. 443, 167–175.
Wang, Z., Fang, Q., Li, J., Liu, B., Liu, Y., 2018b. Effect of lattice distortion on solid solution strengthening of BCC high-entropy alloys. J. Mater. Sci. Technol. 34, 349–354.
Wang, Z., Liu, P., Xiao, Y., Cui, X., Hu, Z., Chen, L., 2019. A data-driven approach for process optimization of metallic additive manufacturing under uncertainty. J. Manuf. Sci. Eng. 141, 081004.
Wei, H., Elmer, J., DebRoy, T., 2016. Origin of grain orientation during solidification of an aluminum alloy. Acta Mater 115, 123–131.
Xing, H., Jing, H., Dong, X., Wang, L., Han, Y., Hu, R., 2022. Cellular growth during rapid directional solidification: insights from quantitative phase field simulations. Mater. Today Commun. 30, 103170.
Xu, X., Ding, H., Huang, H., Liang, H., Chen, R., Guo, J., Fu, H., 2021. Microstructure formation and columnar to equiaxed transition during cold crucible directional solidification of a high-Nb TiAl alloy. J. Mater. Res. Technol. 11, 2221–2234.
Xu, Z., Zhang, H., Du, X., He, Y., Luo, H., Song, G., Mao, L., Zhou, T., Wang, L., 2020. Corrosion resistance enhancement of CoCrFeMnNi high-entropy alloy fabricated by additive manufacturing. Corros. Sci. 177, 108954.
Yao, W., Xia, M., Zeng, L., Ge, X., Qian, M., Wang, Y., Lu, W., Fu, Y., Xie, H., Xiao, T., 2019. Atomic structural competition in the Al 85.5 Ni 9.5 La 5 alloy during liquid-to-solid transition. Metall. Mater. Trans. A 50, 3441–3445.
Yi, P., Locker, C.R., Rutledge, G.C., 2013. Molecular dynamics simulation of homogeneous crystal nucleation in polyethylene. Macromolecules 46, 4723–4733.
Yousefian, P., Tiryakioğlu, M., 2018. Pore formation during solidification of aluminum: reconciliation of experimental observations, modeling assumptions, and classical nucleation theory. Metall. Mater. Trans. A 49, 563–575.
Zhakeyev, A., Wang, P., Zhang, L., Shu, W., Wang, H., Xuan, J., 2017. Additive manufacturing: unlocking the evolution of energy materials. Adv. Sci. 4, 1700187.
Zhang, D., Qiu, D., Gibson, M.A., Zheng, Y., Fraser, H.L., StJohn, D.H., Easton, M.A., 2019a. Additive manufacturing of ultrafine-grained high-strength titanium alloys. Nature 576, 91–95.
Zhang, H., Zhao, Y., Cai, J., Ji, S., Geng, J., Sun, X., Li, D., 2021a. High-strength NbMoTaX refractory high-entropy alloy with low stacking fault energy eutectic phase via laser additive manufacturing. Mater. Design 201, 109462.
Zhang, H., Zhu, H., Nie, X., Yin, J., Hu, Z., Zeng, X., 2017. Effect of Zirconium addition on crack, microstructure and mechanical behavior of selective laser melted Al-Cu-Mg alloy. Scr. Mater. 134, 6–10.
Zhang, T., Huang, Z., Yang, T., Kong, H., Luan, J., Wang, A., Wang, D., Kuo, W., Wang, Y., Liu, C.T., 2021b. In situ design of advanced titanium alloy with concentration modulations by additive manufacturing. Science 374, 478–482.
Zhang, Y., Liu, H., Mo, J., Wang, M., Chen, Z., He, Y., Yang, W., Tang, C., 2019b. Atomic-level crystallization in selective laser melting fabricated Zr-based metallic glasses. Phys. Chem. Chem. Phys. 21, 12406–12413.
Zhao, C., Wang, Z., Li, D., Kollo, L., Luo, Z., Zhang, W., Prashanth, K.G., 2021. Selective laser melting of Cu–Ni–Sn: a comprehensive study on the microstructure, mechanical properties, and deformation behavior. Int. J. Plast. 138, 102926.
Zhao, X., Wei, Q., Gao, N., Zheng, E., Shi, Y., Yang, S., 2019. Rapid fabrication of TiN/AISI 420 stainless steel composite by selective laser melting additive manufacturing. J. Mater. Process. Technol. 270, 8–19.
Zhong, L., Wang, J., Sheng, H., Zhang, Z., Mao, S.X., 2014. Formation of monatomic metallic glasses through ultrafast liquid quenching. Nature 512, 177–180.
Żydek, A., Wermiński, M., Trybula, M.E., 2021. Description of grain boundary structure and topology in nanocrystalline aluminum using Voronoi analysis and order parameter. Comput. Mater. Sci. 197, 110660.